

**A THESIS SUBMITTED TO  
THE GRADUATE SCHOOL OF NATURAL AND APPLIED SCIENCES  
OF ÇANKIRI KARATEKİN UNIVERSITY**

**ENHANCING PHOTOVOLTAIC PERFORMANCE OF WO<sub>3</sub>-  
DOPED InZnO FILMS BY PLD TECHNIQUE FOR PEROVSKITE  
SOLAR CELL**

**IN PARTIAL FULFILLMENT OF THE REQUIREMENTS  
FOR  
THE DEGREE OF MASTER OF SCIENCE  
IN  
PHYSICS**

**BY**

**SABAH NOORI ABDFATTAH AL-BAYATI**

**ÇANKIRI**

**2023**

ENHANCING PHOTOVOLTAIC PERFORMANCE OF WO<sub>3</sub>-DOPED InZnO FILMS  
BY PLD TECHNIQUE FOR PEROVSKITE SOLAR CELL

By Sabah Noori Abdulfattah AL-BAYATI

February 2023

We certify that we have read this thesis and that in our opinion it is fully adequate, in scope and in quality, as a thesis for the degree of Master of Science

**Advisor** : Prof. Dr. Sebahaddin ALPTEKİN

**Co-Advisor** : Asst. Prof. Dr. Ghusoon Hameed MOHAMMED

**Examining Committee Members:**

**Chairman** : Prof. Dr. Şemsettin ALTINDAL  
Physics  
Gazi University

**Member** : Prof. Dr. Sebahaddin ALPTEKİN  
Physics  
Çankırı Karatekin University

**Member** : Prof. Dr. Çiğdem YÜKSEKTEPE ATAOL  
Physics  
Çankırı Karatekin University

**Approved for the Graduate School of Natural and Applied Sciences**

**Prof. Dr. İbrahim ÇİFTÇİ**  
**Director of Graduate School**

**I hereby declare that all information in this document has been obtained and presented in accordance with academic rules and ethical conduct. I also declare that, as required by these rules and conduct, I have fully cited and referenced all material and results that are not original to this work.**

**Sabah Noori Abdulfattah AL-BAYATI**

## ABSTRACT

# ENHANCING PHOTOVOLTAIC PERFORMANCE OF WO<sub>3</sub>-DOPED InZnO FILMS BY PLD TECHNIQUE FOR PEROVSKITE SOLAR CELL

Sabah Noori Abdulfattah AL-BAYATI

Master of Science in Physics

Advisor: Prof. Dr. Sebahaddin ALPTEKİN

Co-Advisor: Asst. Prof. Dr. Ghusoon Hameed MOHAMMED

February 2023

This study investigated the effect of composing indium-zinc oxide IZO with tungsten oxide and prepared as a thin film by pulsed laser deposition technique on the characteristics of the deposited IZO thin films. The X-Ray Diffraction (XRD) shows to compose of the IZO with different ratios of WO<sub>3</sub>, causing the appearance of hybrid ZnO and WO<sub>3</sub> phases. Doping with WO<sub>3</sub> highly effect lattice constants, crystalline size, and lattice strain. The crystalline size reduced with increasing the WO<sub>3</sub> to 15 %, while the opposite behavior appeared for the lattice strain and fluctuation of the lattice constants due to the incorporation of some of the W atoms within the ZnO lattice. The optical absorption is slightly increased, and the energy bandgap is reduced (from 2.8 to 2.1 eV) with the WO<sub>3</sub> content. Hall Effect measurement shows that all films were n-type, charge carrier mobility decreased, while the mobility reduced, and the conductivity enhanced with WO<sub>3</sub> content. The I-V characteristics of the ZnO/p-Si, IZO/p-Si and IZO: WO<sub>3</sub>/ p-Si heterojunction at different WO<sub>3</sub> ratios show photovoltaic behavior. Here, with a 15% contribution, it is the sample with the highest efficiency ( $\eta=5.60\%$ ).

**2023, 73 pages**

**Keywords:** Perovskite solar cells, Indium–zinc oxide, PLD technique

## ÖZET

# PEROVSKİTE GÜNEŞ PİLİ İÇİN PLD TEKNİĞİ İLE WO<sub>3</sub> KATKILI InZnO FİMLERİNİN FOTOVOLTAİK PERFORMANSINI GELİŞTİRME

Sabah Noori Abdulfattah AL-BAYATI

Fizik, Yüksek Lisans

Tez Danışmanı: Prof. Dr. Sebahaddin ALPTEKİN

Eş Danışman: Dr. Öğr. Üyesi Ghusoon Hameed MOHAMMED

Şubat 2023

Bu çalışmada, darbeli lazer biriktirme tekniği ile ince bir film olarak hazırlanan ve tungsten oksit ile indiyum-çinko oksit IZO'nun birleştirilmesinin, biriktirilen IZO ince filmlerinin özelliklerine etkisi araştırılmıştır. X-ışını kırınımı (XRD), IZO'nun farklı WO<sub>3</sub> oranlarıyla oluşturduğunu ve karışık ZnO ve WO<sub>3</sub> fazlarının ortaya çıkmasına neden olduğunu göstermektedir. WO<sub>3</sub> ile katkı, kafes sabitlerini, kristal boyutunu ve kafes gerilmesini oldukça etkiler. WO<sub>3</sub>'ün %15'e yükseltilmesiyle kristal boyutu azalırken, ZnO kafesi içine bazı W atomlarının dahil edilmesinden dolayı kafes gerilmesi ve kafes sabitlerinin dalgalanması için zıt davranış ortaya çıktı. Optik absorpsiyon biraz artar ve WO<sub>3</sub> içeriği ile enerji bant aralığı azalır (2,8'dan 2,1 eV'a). Hall Etkisi ölçümü, tüm filmlerin n-tipi olduğunu, yük taşıyıcı hareketliliğinin azaldığını ve WO<sub>3</sub> içeriği ile iletkenliğin arttığını göstermektedir. ZnO/p-Si, IZO/p-Si ve IZO: WO<sub>3</sub>/p-Si heteroekleminin farklı WO<sub>3</sub> oranlarında katkıları ile I-V özellikleri fotovoltaiik davranış göstermiştir. Burada %15 katkı ile verimi en yüksek olan ( $\eta=5,60$ ) numunedir.

**2023, 73 sayfa**

**Anahtar Kelimeler:** Perovskit güneş pilleri, İndiyum-çinko oksit, PLD tekniği

## **PREFACE AND ACKNOWLEDGEMENTS**

I would like to thank my thesis advisor Prof. Dr. Sebahaddin ALPTEKİN for his patience, guidance, and understanding. I would like to thank Prof. Dr. Şemsettin ALTINDAL and appreciate his efforts. I thank Prof. Dr. Çiğdem YÜKSEKTEPE ATAOL. I would like to thank Asst Prof. Dr.Ghusoon Hameed MOHAMMED, and last I would thank my family to their support and their love.

**Sabah Noori Abdulfattah AL-BAYATI**

**Çankırı-2023**



## CONTENTS

<b>ABSTRACT</b> .....	<b>i</b>
<b>ÖZET</b> .....	<b>ii</b>
<b>PREFACE AND ACKNOWLEDGEMENTS</b> .....	<b>iii</b>
<b>CONTENTS</b> .....	<b>iv</b>
<b>LIST OF SYMBOLS</b> .....	<b>vi</b>
<b>LIST OF ABBREVIATIONS</b> .....	<b>vii</b>
<b>LIST OF FIGURES</b> .....	<b>viii</b>
<b>LIST OF TABLES</b> .....	<b>x</b>
<b>1. INTRODUCTION</b> .....	<b>1</b>
1.1 Literature Review .....	3
1.2 Aim of the Research.....	7
<b>2. THEORETICAL PART</b> .....	<b>8</b>
2.1 Semiconductor.....	8
2.2 Thin Films Deposition Techniques.....	9
2.3 Pulsed Laser Deposition .....	11
2.4 Structural Properties.....	13
2.5 Atomic Force Microscope (AFM).....	14
2.6 Optical Properties of Semiconductors .....	15
2.6.1 Optical transition .....	16
2.7 Electrical Properties of Semiconductors.....	17
2.7.1 Hall effect.....	18
2.8 Solar Cells.....	20
2.8.1 Fundamental requirements for solar cell .....	20
2.8.2 Parameters of a solar cell .....	23
2.9 Zinc Oxide.....	25
2.10 Indium Oxide.....	26
2.11 Fundamental Properties of Tungsten Oxide.....	28
<b>3. EXPERIMENTAL WORK AND PROCEDURE</b> .....	<b>31</b>
3.1 Materials.....	32
3.2 Pellet Samples Preparation.....	32
3.3 Substrate Preparation.....	33

3.3.1 Glass substrate cleaning procedure .....	33
3.4 Silicon Substrate .....	34
3.4.1 Photochemical etching.....	34
3.5 Thin Films Preparation .....	35
3.5.1 The laser source .....	36
3.6 Thin Films Characterization.....	36
3.6.1 The thickness of thin films .....	37
3.6.2 X-ray diffraction (XRD).....	37
3.6.3 Atomic force microscopy (AFM).....	38
3.6.4 UV-visible absorbance.....	38
3.6.5 Hall effect measurements .....	38
3.7 Heterojunction Fabrication .....	39
3.7.1 Mask preparation .....	39
3.8 The I-V Characteristics for the Heterojunctions .....	40
<b>4. RESULTS AND DISCUSSION.....</b>	<b>42</b>
4.1 Introduction.....	42
4.2 Structural properties.....	42
4.3 Atomic Force Microscopy .....	48
4.4 EDX Analysis.....	50
4.5 Furrier Transform Infra-Red Spectroscopy .....	53
4.6 Optical Properties.....	54
4.7 Hall Effect Measurements .....	57
4.8 I-V Characteristics.....	59
<b>5. CONCLUSIONS AND RECOMMENDATION.....</b>	<b>62</b>
5.1 Conclusions .....	62
5.2 Recommendations for Future Works.....	63
<b>REFERENCES.....</b>	<b>64</b>
<b>CURRICULUM VITAE.....</b>	<b>73</b>

## LIST OF SYMBOLS

C.S	Crystalline size
$d_{hkl}$	Inter-atomic distances
$E_g$	Energy gap
H	Planck constant
I	Intensity
$I_H$	Hall current
$I_m$	Current at maximum power
$I_{Sc}$	Short circuit current
k	Wave vector
$N_H$	Carrier's concentration
$P_m$	Maximum power
q	Carrier's charges
$R_H$	Hall resistance
$R_s$	Series resistance
$R_{sh}$	Shunt resistance
$V_H$	Hall voltage
$V_m$	The voltage at maximum power
$V_o$	Open circuit voltage
x	Film thickness
$\alpha$	Absorption coefficient
$\beta$	Diffraction line breadth
$\epsilon$	Lattice strain
$\eta$	Solar cell efficiency
$\theta$	Diffraction angle
$\lambda$	Wavelength
$\mu_e$	Electrons mobility
$\mu_h$	Hole mobility
$\sigma$	Electrical conductivity

## LIST OF ABBREVIATIONS

AFM	Atomic force microscope
C.B.	Conducting band
EDX	Energy dispersive x-ray spectroscopy
FTIR	Fourier transform infrared spectrometer
FWHM	The full width at half maximum
PLD	Pulse Laser Deposition
$R_H$	Hall effect coefficient
$V_H$	Hall voltage
V.B	Valence band
XRD	X-ray diffraction



## LIST OF FIGURES

Figure 2.1	Schematic diagram of the bandgaps for insulators, semiconductors, and conductors, illustrating their various sizes (Chopra and Maini 2010) .....	8
Figure 2.2	Classification of preparation techniques of nanoparticles (Horikoshi and Serpone 2013) .....	10
Figure 2.3	Scheme of the laser interaction with targets (Barhdadi <i>et al.</i> 2012) .....	11
Figure 2.4	Scheme of PLD setup (Chrissey and Hubler 1994) .....	12
Figure 2.5	Scheme of AFM probe scanning (Kalantar-Zadeh and Fry 2008) .....	15
Figure 2.6	Types of electrical transitions over the energy bandgap (a) Permitted, (b) Prohibited, (c) Permitted, and (d) Prohibited (Greiner 1961) .....	17
Figure 2.7	Schematic of Hall Effect (Rai and Raj 2004) .....	18
Figure 2.8	Solar cell's dark and illuminated I-V curve .....	21
Figure 2.8 (b)	Solar panel configuration .....	21
Figure 2.9	Equivalent circuit of a solar cell .....	21
Figure 2.10	I-V Curve of the solar cell in dark and under light .....	23
Figure 2.11	Zinc oxide structure .....	26
Figure 2.10	Indium oxide crystal structure .....	27
Figure 3.1	Scheme for experimental work .....	31
Figure 3.2	The stainless steel mold for pressing the pellet targets .....	33
Figure 3.3	Photograph of the setup of the photochemical etching process .....	35
Figure 3.4	Scheme of the PLD setup .....	36
Figure 3.5	Optical thickness measurement .....	37
Figure 3.6	Schematic diagram for the prepared photovoltaic device .....	39
Figure 3.7	On the films for (A) the Hall effect electrode and (B) the solar cell mesh electrode, the white masks denote the aluminium electrodes .....	40
Figure 3.8	IZO:WO <sub>3</sub> /p-Si heterojunction samples at different WO <sub>3</sub> contents (A) 0, (B) 10%, (C) 20%, (D) 30%, and (E) 40% .....	40
Figure 3.9	Schema of I-V characteristics examination circuit for the photovoltaic device .....	41
Figure 4.1	XRD patterns for the ZnO thin films on glass slides .....	43
Figure 4.2	XRD patterns for pure IZO films and that doped with different contents of WO <sub>3</sub> .....	44
Figure 4.3	Crystalline size and lattice strain variation with the WO <sub>3</sub> content .....	47
Figure 4.4	Variation of lattice constants for ZnO with the WO <sub>3</sub> content .....	47
Figure 4.5	AFM two and three dimensional images for ZnO, IZO, and that doped with different contents of WO <sub>3</sub> thin films deposited on glass substrate ..	48
Figure 4.6	EDX analysis for ZnO, IZO, and that doped with different contents of WO <sub>3</sub> thin films .....	50
Figure 4.7	Variation of O atomic percentage with the WO <sub>3</sub> content .....	52

Figure 4.8 FTIR patterns for ZnO, IZO, and that doped with different contents of WO <sub>3</sub> thin films .....	54
Figure 4.9 UV-vis optical absorption for ZnO, IZO, and that doped with different contents of WO <sub>3</sub> thin films.....	55
Figure 4.10 Absorption coefficient as a function of wavelength for ZnO, IZO, and that doped with different contents of WO <sub>3</sub> thin films .....	56
Figure 4.11 $(\alpha h\nu)^2$ versus $(h\nu)$ for ZnO, IZO, and that doped with different contents of WO <sub>3</sub> thin films .....	57
Figure 4.12 Charge carrier concentration and their mobility variation with the WO <sub>3</sub> contents in the IZO thin films samples.....	58
Figure 4.13 DC conductivity variation with the WO <sub>3</sub> contents in the IZO thin films samples .....	59
Figure 4.14 I-V characteristics for ZnO, IZO, and IZO: WO <sub>3</sub> /P-Si heterojunctions..	60



## LIST OF TABLES

Table 2.1 Some physical properties of ZnO (Ngom <i>et al.</i> 2009) .....	25
Table 2.2 Some physical properties of indium oxied .....	28
Table 2.3 Some physical properties of WO <sub>3</sub> (Ge <i>et al.</i> 2018).....	29
Table 3.1 Chemical materials .....	32
Table 4.1 XRD parametersfor the ZnO thin films on glass slides.....	43
Table 4.2 XRD patterns for pure IZO films and that doped with different contents of WO <sub>3</sub> .....	45
Table 4.3 The effect of WO <sub>3</sub> content on the lattice parameters and lattice strain for the IZO thin films .....	46
Table 4.4 AFM results (Average Diameter, and RMS roughness) for ZnO, IZO, and that doped with different contents of WO <sub>3</sub> thin films. ....	48
Table 4.5 Wt% and atom % for ZnO, IZO, and that doped with different contents of WO <sub>3</sub> thin films .....	52
Table 4.6 FTIR bands for ZnO, IZO, and that doped with different contents of WO <sub>3</sub> thin films.....	53
Table 4.7 The optical band gap for ZnO, IZO-WO <sub>3</sub> thin films at different ratios.....	57
Table 4.8 Hall effect parameters for ZnO, IZO, and that doped with different contents of WO <sub>3</sub> thin films .....	58
Table 4.9 Solar cell characterization for ZnO, IZO, and IZO: WO <sub>3</sub> /P-Si heterojunctions .....	60

## 1. INTRODUCTION

Nanotechnology is the science of studying the production, characterization, and characteristics of nanomaterials with at least one characteristic dimension smaller than 100 nm. Nanomaterials have new behaviours than bulk samples due to their small size, due to increasing their surface area compared with the bulk materials, or due to other fundamental size effects. As the material size is reduced to the nano-scale, the features of various physical phenomena, such as electron and phonon mean free paths, become clear. The result is that properties can deviate from bulk substances (Khan *et al.* 2019).

Recently, transparent nanostructured metal oxides have gained significant interest due to their varying properties related to their bulk shape, providing promising applications in many technology areas. The preparation of high-quality nanostructures with well-organized dimensions and morphology is a paramount necessity to improve device performance in diverse requirements of sensor materials and pharmacology (Stadler 2012).

The research on nanomaterials has been revolutionized in the past few years due to their attractive properties compared to similar primary materials. These properties fall into physical, chemical, catalytic, and visual. Metal oxide nanostructures are among the nanomaterials. Scientists are particularly interested in using them to create diverse optical, biochemical, and biological nanodevices. Nanotechnology manufactures delicate and sensitive nanodevices based on nanomaterials (Paramasivam *et al.* 2021).

Transparent conductive metal oxides (TCOs) films are an essential component of many photovoltaic devices that use transparent electrodes in different optoelectronic devices (Minami 2005). Light-emitting diodes (Abrutis *et al.* 2007) and photodetectors (Khusayfan *et al.* 2016). These electrodes have low resistance in addition to high light transparency. The finest and most commercialised TCOs thin films are based on cations with filled d-shells, such as  $Zn^{2+}$ ,  $Cd^{2+}$ ,  $In^{3+}$ , and  $Sn^{4+}$ , which display n-type character. (Mason *et al.* 2010).

The interest in nanotechnology has increased owing to the unique properties that enable it to be applied in many scientific fields. It is employed in different technologies and industries and has also entered the medical and pharmaceutical fields (Chen *et al.* 2013). This is because of its high chemical reactivity, lightweight, tiny size, large surface area, and high stability (Xu *et al.* 2018).

Zinc oxide, one of the most prominent nanomaterials, has received a lot of interest from the scientific and medical sectors due to its important role in many biomedical and antimicrobial applications, as well as its unique chemical and physical properties (Jiang *et al.* 2018). Such as high electrochemical correlation coefficient and high photochemical stability (Saritha *et al.* 2019). Zinc oxide (ZnO) is classified as a group II-VI between ionic and covalent semiconductors. ZnO can be found in one, two, and three-dimensional structures, and the structures are more than others (Napi *et al.* 2020). ZnO shows the wurtzite or rock salt structure (hexagonal symmetry) or (cubic symmetry), but ZnO crystals are more common and stable with wurtzite (Kołodziejczak-Radzimska and Jesionowski 2014).

Zinc oxide is a practice in broad applications such as photovoltaic devices and photocatalysis. Zinc oxide has multiple properties suitable for high technology, such as LED, photovoltaic sensors, chemical and biological sensors, and energy accumulators: including solar cells, nanogenerators, and electromagnetics, due to its high chemical, thermal, electronic, photoelectric, and piezoelectric properties (Witkowski 2018).

Nano-zinc oxide found use in a variety of other fields than those above. Recently, however, the field of medicine has seen a remarkable development in the use of nanoparticles, where nanoparticles can be manufactured in a specific shape and size for the desired purpose, as there is the possibility of offering new approaches to disease defense that have been difficult to focus on due to their size limitations (Jiang *et al.* 2018). There is a growing need to find metal oxide NPs that are safe for the environment due to their widespread therapeutic uses (Sirelkhatim *et al.* 2015).

## 1.1 Literature Review

Tsai et al. (2018) thin films of indium zinc oxide were produced by DC magnetron sputtering from ceramic oxide targets of  $\text{In}_2\text{O}_3:\text{ZnO}$  with 7:3 wt ratio onto glass slides at room temperature, and their structural, optical, and electrical characteristics were investigated as a function of film thickness. The IZO films exhibit an amorphous structure with low roughness. They were increasing thickness, cause to convert to semi-crystalline. Thick samples contained higher concentration and mobility (higher conductivity) but had high visible light absorbance. As the material's thickness increased, the Urbach energy decreased, shifting the bandgap to higher energies. The optimum thickness of the IZO film was calculated to be 800 nm using the figure of merit calculations (Tsai *et al.* 2018).

Silva-Lopez *et al.* (2018) studied, deposited high transmittance IZO polycrystalline thin films changed types of substrates at room temperature by rf magnetron sputtering from mixed powders target. The IZO showed n-type conductivity. Several orders of magnitude enhance the electrical conductivity, and the carrier concentration increases with the In content within the ZnO lattice. The best mobility obtained was  $27.7 \pm 0.8 \text{ cm}^2\text{V}^{-1}\text{s}^{-1}$  for an IZO on flexible substrates (Silva-Lopez *et al.* 2018).

Muru et al. (2018) Using a simple sol-gel spin coating procedure and annealing at  $500^\circ\text{C}$  for an hour in a nitrogen atmosphere, they were able to manufacture Al and In doped ZnO transparent conducting oxide thin films for solar cell applications. XRD analysis reveals that annealing has improved the crystallinity of ZnO, revealing its characteristic hexagonal wurtzite structure. Analysis of surface morphology reveals that Al-doped ZnO has the smoothest surfaces compared to undoped films. The prepared film samples showed transmittance larger than 96% of visible light (Muru *et al.* 2018).

Winkler *et al.* (2018), prepared solar cells based on a  $\text{Cu}_2\text{O}$  absorber, transparent IZO contact, with buffer layers of ZnO or  $\text{Zn}_{1-x}\text{Mg}_x\text{O}$  by ultrasonic spray pyrolysis.

Top contacts made of graphite paste finished the cells. The developed spray pyrolysis produced highly conductive and transparent IZO, and the energy band gap (3.28-3.50 eV) exhibits a linear dependency on Mg concentration (0-16 mol%). With a short-circuit current density of 3.76 mA/cm<sup>2</sup>, an open-circuit voltage of 0.34 V, and a fill factor of 52.7%, the photovoltaic efficiency rose to 0.67% (Winkler *et al.* 2018).

Djelloul *et al.* (2018) ZnO thin films were deposited on glass substrates through ultrasonic spray pyrolysis, and their structural, morphological, optical, and electrical characteristics were investigated (USP). To further understand the differences between undoped and (Al, In) doped ZnO thin films, we characterized them using XRD, SEM, optical absorption method (UV), and the four-point probe technique. The films were discovered to be polycrystalline with a wurtzite structure and exhibit (101) preferred growth, according to structural analyses. Additionally, we experiential that the favoured orientation is independent of the dopant's composition. Al and In dopants changed the bandgaps (E<sub>g</sub>), which ranged from 3.35 to 3.37 eV (Djelloul *et al.* 2018).

Wang *et al.* (2018), prepared high-quality IZO by spin-coating method for the electron transport layer. This upgraded IZO ETL film achieved a high power conversion efficiency (PCE) of 16.25%, delivering an absolute efficiency gain of 2.42 percent above TiO<sub>2</sub>-based PVSC (13.83 per cent). It also demonstrated a steady-state efficiency of 15.8% with little hysteresis (Wang *et al.* 2018).

Chiang *et al.* (2018), prepared bifacial luminous perovskite solar cells, two PSCs based on polyunsaturated tin oxide (FTO) and ultra-thin substrates, and a transparent IZO layer. With a 1 cm<sup>2</sup> area and dual-illuminated PSCs, the tandem Si/perovskite solar cell system achieves a respectable power efficiency of 19.51 per cent. Using the sprayed Ti metal as a substrate, screening PSCs without an FTO substrate has been demonstrated. Good use of low-cost and lightweight devices other than FTO can be seen in devices using a Ti cathode coating on a chip and ultrathin glass, which can provide 13.5% and 13.6% PCE, respectively (Chiang *et al.* 2018).

Liu *et al.* (2019), an aqueous solution was used to create extremely transparent conductive Al-doped ZnO thin films, which were then exposed to UV light and annealed at 200°C. The results indicated that the visible range had a high transmittance of 85% and a low electrical resistance of  $4.8 \times 10^{-3} \Omega$ . UV irradiation might improve conductivity by reducing oxygen flaws and releasing free carriers at interfaces. Cu<sub>2</sub>ZnSnS<sub>4</sub>-based photovoltaics with optimum Al-ZnO thin films as top electrodes achieved the highest efficiency of 7.15% (Liu *et al.* 2019).

Winkler *et al.* (2019), they investigated the effect of substrate temperature and deposition rate on the physical properties of IZO films by ultrasonic spray pyrolysis technique. Low-cost and low-toxicity precursors were used. Spatially homogeneous IZO films were achieved with high transparency (>80%) and low resistivity ( $3.8 \times 10^{-3} \Omega \cdot \text{cm}$ ) for 1800 nm thickness, with high carrier concentration and mobility (Winkler *et al.* 2019).

Le *et al.* (2019), achieved mobility of 410 cm<sup>2</sup>/V.s in an amorphous C60-doped -IZO thin-film without resorting to high annealing temperatures, which are unfavorable for use with flexible substrates. With just a 250°C anneal, thin-film transistors may benefit greatly from bulk charge-transfer doping with a mixed starting solution. Moreover, 1% optimized doping increased device stability under a bias stress scenario (Le *et al.* 2019).

Lin *et al.* (2019), examined the impact of nickel (Ni)-doping on the electrical characteristics of amorphous IZO channel layers made by rf magnetron sputtering. The decrease in oxygen vacancies is responsible for the threshold voltage shifting to the positive direction with increased Ni-doping content. The 6.6 at % Ni percentage exhibit mobility of 30.2 cm<sup>2</sup>/v.sec. Ni is an effective carrier suppressor for IZO thin film (Lin *et al.* 2019).

Vasile *et al.* (2020), The IZO and Al-doped IZO thin films on glass substrates were created using RF magnetron sputtering. Researchers looked at how RF power affected the structure, morphology, and optics of the material. X-ray diffraction showed that pure samples were in an amorphous phase, whereas Al-doped samples retained ZnO's

Wurtzite structure. All of the films that were tested with an AFM had smooth surfaces. After being doped, the optical transmission spectra became 70% transparent, an increase of 10%. To improve crystallinity, doping may be used in place of heat treatment (Vasile *et al.* 2020).

Shaheera *et al.* (2020), RF sputtering with magnetron methods was used to create undoped and in-doped ZnO nanostructured films from pressed powder targets. They used AFM, XRD, and EDS to investigate surface morphology, crystal structure, and elemental analyses. Having indium doping, the peak intensities of (100), (002), and (101) changed noticeably in all of the films with hexagonal wurtzite structures. The EDS validated the inclusion of In into the ZnO films. The optical investigations revealed an absorption edge of about 380 nm and high transmittance of over 90% in the UV-vis band. With In content, the bandgap widens from 3.27 to 3.42 eV (Shaheera *et al.* 2020).

Cho *et al.* (2021), prepared a hafnium-IZO composite at different Hf concentrations (from 0 to 100 at%) for NO<sub>2</sub> gas sensor application. The sample prepared at 15% doping concentration shows higher selectivity, long-term stability, and advanced responsiveness than the undoped IZO thin films. X-ray diffraction (XRD), transmission electron microscopy (TEM), and X-ray photoelectron spectroscopy are used to study the materials' microstructures and chemical states (XPS). The findings indicate a relationship between the concentration of oxygen vacancies produced at this doping ratio and a gas reaction (Cho *et al.* 2021).

Lu *et al.* (2021), investigated the effect of a copper alloy source/drain electrode in amorphous Nd-doped IZO thin-film transistors and compared it to that of an Al electrode. According to X-ray photoelectron spectroscopy examination of the contact interface's depth profile, zirconium (Zr) oxide and chromium (Cr) oxide aggregates at the S/D electrode/active layer contact, perhaps serving as a barrier to stray free electron carriers (XPS) (Lu *et al.* 2021).

Dhamodharan *et al.*(2021), they deposited very transparent ZnO and IZO thin films on ITO substrates. The XRD analysis supported the ZnO wurtzite structure. The pristine ZnO had a granular and porous structure, whereas the IZO thin films had a nanofiber network structure, according to the FESEM pictures. As assessed by AFM, the key to getting high performance in PV applications was the porosity structure with lower roughness. High transmittance was demonstrated using IZO sheets in the visible spectrum. For 1.5 per cent of In dopant, a minimum resistivity of  $1.22 \cdot 10^3 \text{ cm}$  and a maximum electron concentration of  $10.74 \cdot 10^{19} \text{ cm}^3$  were attained. The DSSC's IZO photoanode's photovoltaic performance demonstrated the most incredible efficiency of 1.09 per cent (Dhamodharan *et al.* 2021).

## 1.2 Aim of the Research

This work aims to fabricate (In-Zn oxide):  $\text{WO}_3/\text{p-Si}$  solar cell by modifying specific characteristics of the IZO films prepared on Si wafer using the PLD method.

The main objectives of this work are

- Initially, preparing IZO by using the PLD technique at different  $\text{WO}_3$  on glass and Si substrates.
- Investigation of the effect of the  $\text{WO}_3$  doped at changed ratios on the structural (using XRD), surface morphology (using AFM), optical characteristics, and electrical behaviour for IZO.
- We are studying the figure of merit of the prepared solar cell.

## 2. THEORETICAL PART

### 2.1 Semiconductor

A substance with electrical conductivity between a conductor and an insulator in magnitude is said to be a semiconductor. This denotes conductivity anywhere between  $10^3$ - $10^{-8}$  S/cm. Due to their widespread usage in several studies and thin-film applications, including electrical devices and solar cell applications, semiconductors have attracted high interest (Zaien *et al.* 2013).

Semiconductors are characterized by structural, optical, or electrical studies and have medium electrical characteristics between metals and insulators. The gap between an electron's valence and conducting band is a bandgap (Kusumawati 2015). Size and existence of this band gap allow for the classification of materials as either conductors, semiconductors, or insulators. Band diagrams, which are diagrams that display these distances, are Figure 2.1. The materials' unique characteristics are partly due to the extent of this band gap. The gap in semiconductors is so tiny that some stimulation can fill it. In this concept, only a small fraction of electrons may cross the conduction band, resulting in a negligible current (Chopra and Maini 2010).

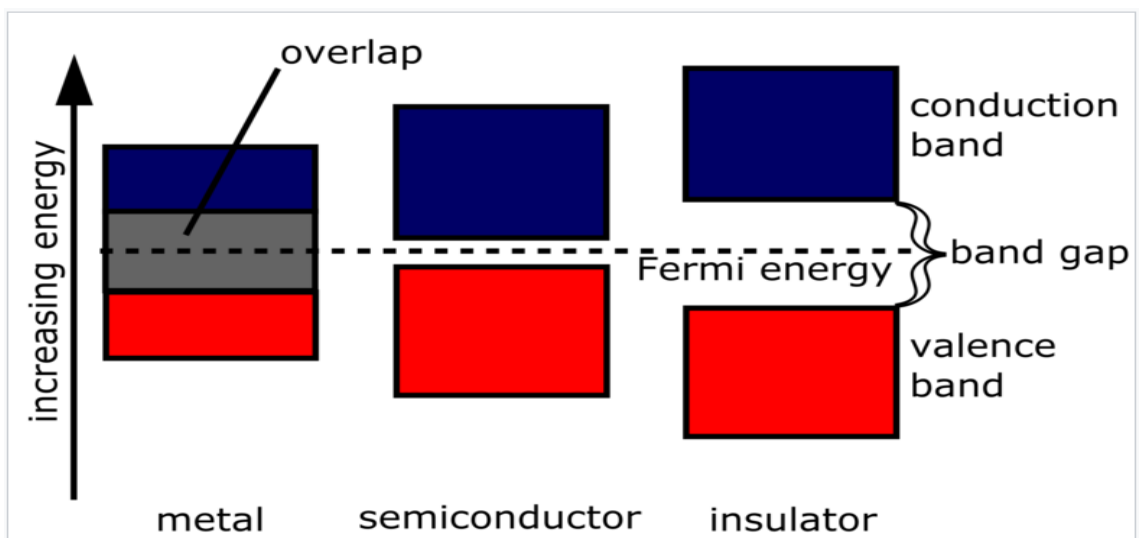


**Figure 2.1** Schematic diagram of the bandgaps for insulators, semiconductors, and conductors, illustrating their various sizes (Chopra and Maini 2010)

Current in a semiconductor is frequently conceptualized as moving either electrons or holes throughout the material's electron structure. An "intrinsic" semiconductor is entirely pure. Doping with other materials can affect a semiconductor's electronic characteristics and conductivity in a controlled way. It is generally known that semiconductors have had an essential role in advancing research in nanoscience and nanotechnology, leading to novel classes of semiconductor nanomaterials with numerous production and uses (Zhang 2017).

Nanoparticles have a restricted size distribution and a minimum dimension range of 1 to 100 nm (Wankhede *et al.* 2013). A cluster of atoms that ranges in size from a few to tens of nanometers and includes a few hundred to tens of thousands of them is known as a nanocrystal. Nanocrystals are alluring and fascinating because they vary from ordinary bulk materials and possess unique qualities. Recently, there has been much research on the fundamental characteristics of semiconductor nanostructures (Koole *et al.* 2014). The quantum confinement effect, which has two main effects, is the effect of nanoscale that is most noticeable. First, when size decreases, the semiconductor material's band gap widens, and discrete energy storage becomes more prevalent (De Mello Donegá 2014).

## **2.2 Thin Films Deposition Techniques**

According to the intended research or scientific necessity, thin films refer to a layer or many atoms of a substance placed on bases made of glass, silicon, aluminium, quartz, etc. (Bel-Hadj-Tahar and Mohamed 2014).

Thin film technology is essential because it is used in many applications, including integrated circuits, anti-reflective coatings, optical communications, solar cells, LED lights, detectors, and other systems and equipment (Acosta 2021).

Metal oxides are opaque when they are present in bulk. To produce transparent conducting oxide (TCO), it must be placed in thin sheets (Bel-Hadj-Tahar and



### 2.3 Pulsed Laser Deposition

The fundamentals of the deposition method have an essential character in the features of the deposited thin films. The PLD method is acceptable for preparing metal oxides with high melting and evaporation temperatures. It is considered a bottom-up approach that entails building the prepared thin films out of sputtering atoms or moles. The deposited samples are chemically identical to the target components' ratios (Rajput 2015).

Three phases make up the PLD technique: vaporizing the laser-assisted material, moving the plasma column containing the various species of ions, neutral atoms, and electrons, and condensing the thin layer on the substrate. These three steps are repeated several times during the deposition process using several laser pulses. The stages of laser interaction with the target material during pulse laser bombardment are depicted in Figure 2.3. Layer-by-layer deposition occurs in a vacuum chamber with several laser pulses (Baghdadi *et al.* 2012).

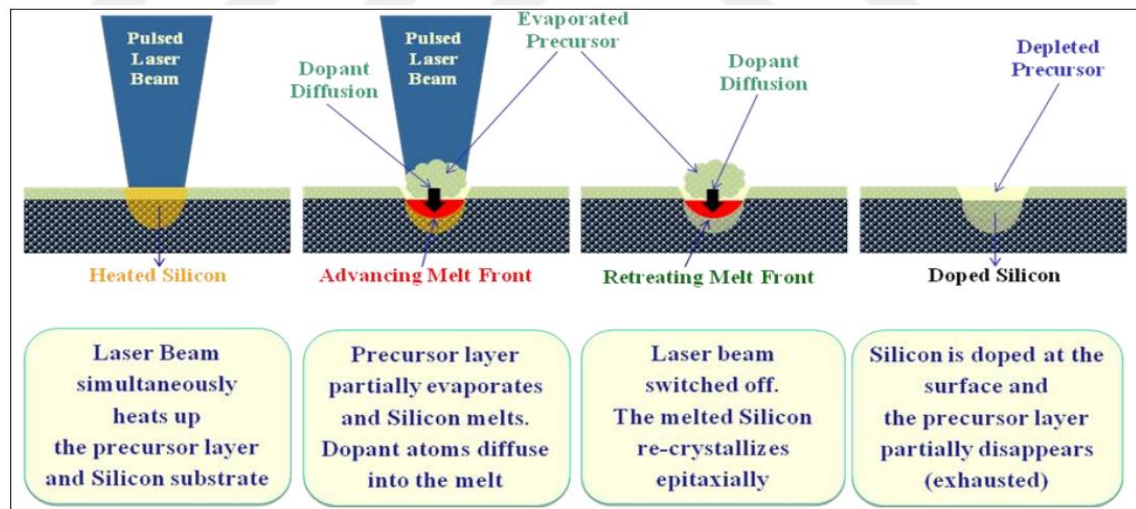


**Figure 2.3** Scheme of the laser interaction with targets (Baghdadi *et al.* 2012)

In numerous investigations, thin films with acceptable specifications are created using the pulsed laser deposition (PLD) technique in a single step. Vacuum vapours are deposited using this method, which depends on physical processes. The pulsed laser is focused on the target of the substance or a mixture of materials that will be deposited. A

small quantity of material is vaporized with each laser pulse, and the plasma column then transports that material to the substrates facing the target. Studies have established this method's efficiency and ease of use for creating thin films for substances with high evaporation temperatures. Each ingredient must exist in the target to precipitate as a combination or complex. As seen in Figure 2.4, the laser wavelength is generally in the infrared range with a nanosecond pulse width that is concentrated inside a very tiny area of the target material (Eason 2007).

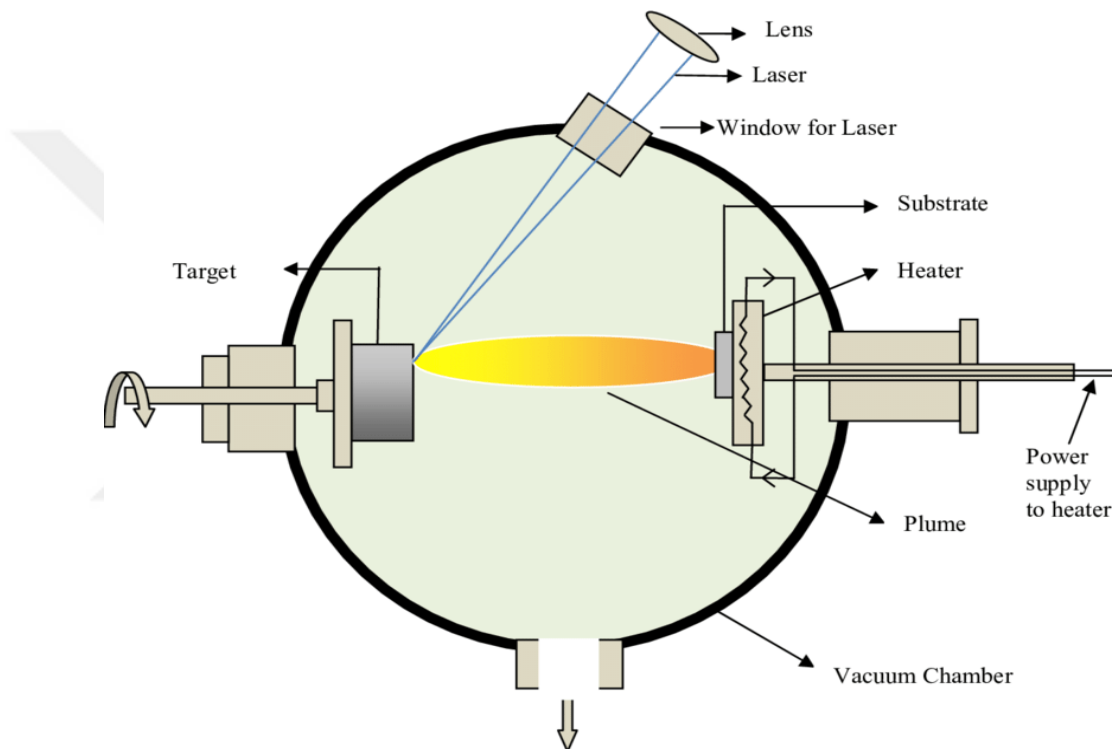


**Figure 2.4** Scheme of PLD setup (Chrisey and Hubler 1994)

The pulsed laser deposition method has a variety of benefits (Lin 2010):

- Crystalline films, which may be sensitive to high temperatures, can be deposited at lower substrate temperatures.
- The laser source is positioned outside the vacuumed isolation chamber to create high-purity films.
- The high degree of controllability of the composition and development process with adjustable gas partial pressure, such as atmospheric oxygen pressure.

- Maybe people can use it to dump various components in various ratios.
- The high energy density of the pulsed laser allows for the deposition of materials with high evaporation points.
- When specific gases are involved in the present, thin films can be formed.
- The targets are smaller than those utilized in other sputtering methods.
- Multi-layers from various targets can be built up.

Despite being employed in numerous scientific fields, the PLD still has several drawbacks:

- The ablation column's tiny zone limits the homogeneity and deposition area. However, this issue may be solved by rotating the substrates.
- Because the ablated column is oriented forward, it is challenging to determine the specimen's thickness.
- Although the target material may deposit large particles on the substrate, this may be prevented by lowering the laser's intensity (Chrisey and Hubler 1994).

## 2.4 Structural Properties

The structural characterization of thin films provides proof of their essential physical characteristics. Thin films' crystallinity must be determined since it is the foundation for all other mechanical, electrical, and optical qualities.

William Bragg proved in 1913 that monochromatic x-rays would diffract as patterns with their angle with the material's surface ( $\theta$ ) following inter-atomic plane lengths ( $d_{hkl}$ ) as shown by the Equation (2.1) (Bragg and Bragg 1918)

$$n \lambda = 2 d_{hkl} \sin \theta \quad (2.1)$$

The lines broadening in the XRD diffraction pattern may be used to measure the crystalline size of the studied material by Scherrer's formula in Equation (2.2) (Scherrer 1918)

$$C.S = \frac{0.9 \lambda}{FWHM \cdot \cos(\theta)} \quad (2.2)$$

When  $\lambda$  is the wave length while the FWHM is full width at half maximum.

## 2.5 Atomic Force Microscope (AFM)

The nano morphology of the sample surface may be effectively studied with atomic force microscopy (AFM) at the nanoscale level. With the aid of a molecularly-influenced nano-tip and a tiny, two-way horizontal movement of the sample surface caused by a piezoelectric phenomenon, surface topography is discovered. AFM is used to investigate semiconductor surfaces that impact a material's characteristics. Solid-state physics applications include figuring out how particles are arranged on a sample's surface as topography, which provides crucial details like average particle size, particle dispersion, and surface roughness (Lang *et al.* 2004).

Van der Waal forces at the tip near the surface cause the flexible cantilever supporting the tapered body to deflect, as illustrated in Figure 2.5. The flexible cantilever's reflective laser beam, turned into data by a light sensor on the rear, detects vertical movement. A picture of the morphology in three dimensions is created using this data. The AFM's contact, tapping, and non-contact styles are distinct. To study surface morphology, contacting and tapping modes were typically employed (Cappella and Dietler 1999).

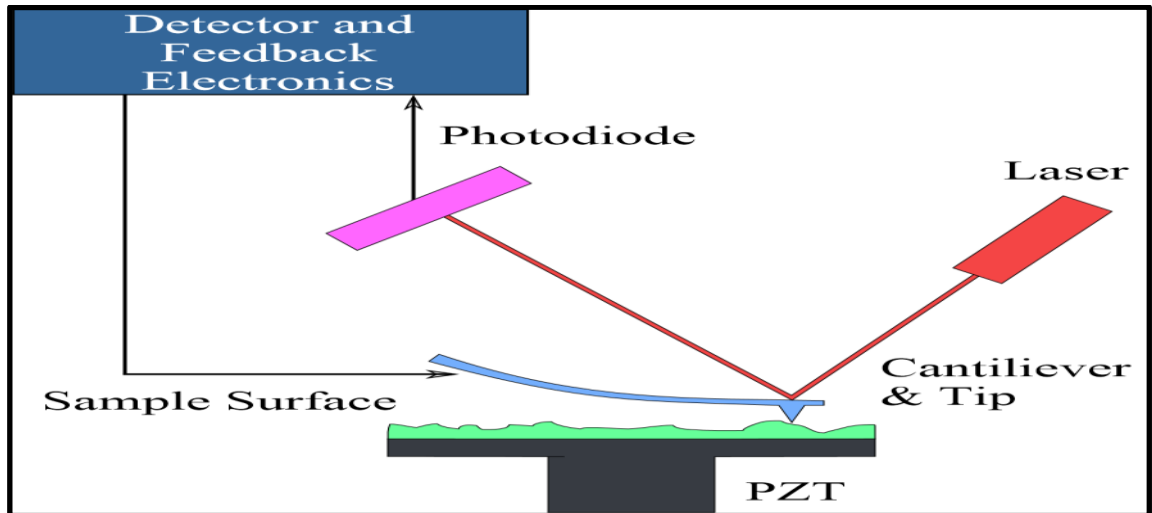


**Figure 2.5** Scheme of AFM probe scanning (Kalantar-Zadeh and Fry 2008)

## 2.6 Optical Properties of Semiconductors

The form of the energy bands and the size of the optical energy gap, which is the energy range between the valence band (V.B.) and the conduction band (C.B.) where electrons are prohibited from existing, determine the optical characteristics of semiconductors (Dresselhaus 2001). Depending on the energy of the light's photons ( $h\nu$ ) about the optical energy gap (where  $\nu$  is the incident photon's frequency and  $h$  is Planck's constant), light may or may not interact with a semiconductor. When a photon's energy is larger or equal to the energy gap, it interacts with the valence electron, excites it to the conduction band, and produces electron-hole pairs that help to conduct electricity (Greiner and Eggers 1989).

The Beer-Lambert Equation (2.3) determines how much light is transmitted through semiconductor sheets (Neamen 1990):

$$I = I_0 \exp(-\alpha t) \quad (2.3)$$

Where  $\alpha$  is the absorption coefficient, and  $t$  is the film thickness. Also, Equation (2.4) can be written as:

$$\alpha = 2.303 A/t \quad (2.4)$$

The relation can determine the incident photon's energy based on its wavelength, Equation (2.5) (Greiner and Eggers 1989)

$$h\nu = \frac{hc}{\lambda} \quad \text{or} \quad h\nu[eV] = \frac{1240}{\lambda [nm]} \quad (2.5)$$

In semiconductors, close to the absorption edge, there are two main categories of electronic transfers: direct and indirect. Each is further broken down into types that are permitted and prohibited. For valence electrons to be hoisted into the conduction band and leave the hall behind, photons must interact with them in each transition (Brodisky 1979).

### 2.6.1 Optical transition

According to Tauc's connection, there are different types of electronic transfers from the valence band (V.B.) to the conduction band (C.B.) Equation (2.6) (Brodisky 1979).

$$\alpha h\nu = B (h\nu - E_g)^r \quad (2.6)$$

Where  $r$  is a constant that changes depending on the kind of electronic transition, with a probability of  $1/2$ ,  $3/2$ ,  $2$ , and  $3$  for direct allowed, direct prohibited, indirect allowed, and indirect forbidden transitions, respectively, the momentum difference is equal to zero ( $\Delta k = 0$ ) in direct transitions between two states because both the valence and conduction bands have the same wave vector value. According to Figure 2.6, this transition may be found in polycrystalline and crystalline semiconductors. The figure illustrates the prohibited transition when the starting state is at its valence level ( $k \neq 0$ ) (Mott and Davis 2012).

When two states in the wave vector ( $\Delta k \neq 0$ ) undergo indirect transformations, the difference in momentum causes the presence of a phonon (crystal vibration), which upholds the idea of momentum conservation.

Since  $E_p$  is the phonon energy,  $h\nu = E_g \pm E_p$  (Greiner 1961), the permitted indirect transformations happen from any position in the valence band to any point in the C.B., while the permitted indirect transitions happen from the top of the V.B. at  $k=0$  (Kazmerski 2012).

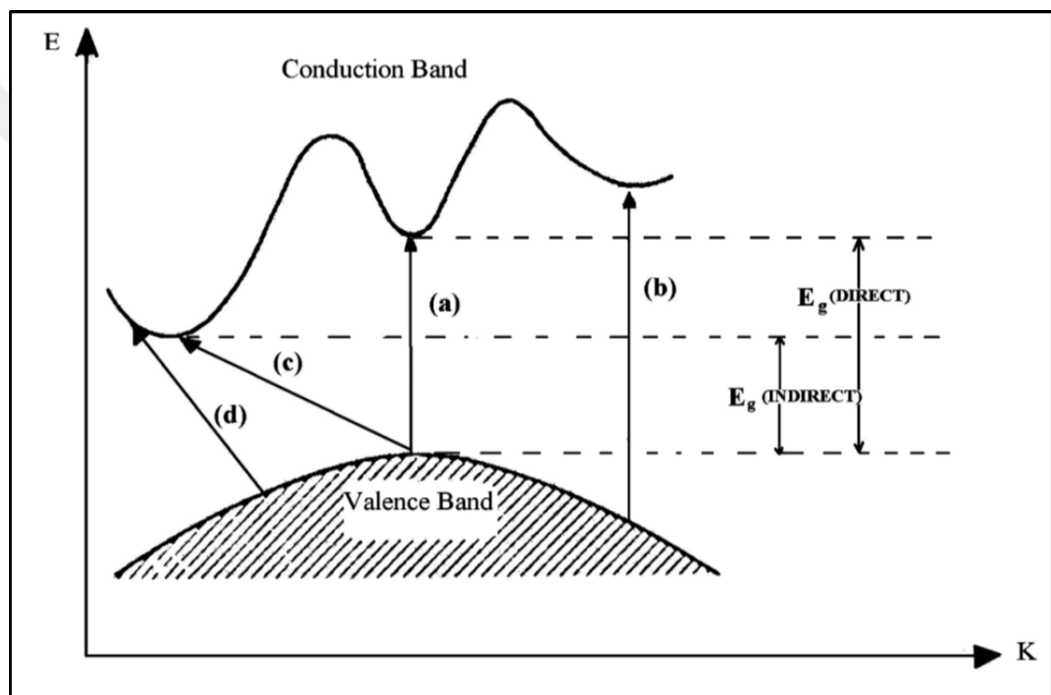


**Figure 2.6** Types of electrical transitions over the energy bandgap (a) Permitted, (b) Prohibited, (c) Permitted, and (d) Prohibited (Greiner 1961)

## 2.7 Electrical Properties of Semiconductors

The electrical characteristics of a substance depend on its atomic arrangement in the solid, its chemical composition, and the presence of defects when the energy gap gives rise to the electron states that affect the material's electrical behaviour. This defect can be reduced by a number of processes, such as the anodization process. Whether a semiconductor is pure, doped, crystalline, or amorphous affects its electrical

characteristics, especially its transport qualities like D.C. electrical conductivity and the Hall effect (Kittel 1955).

### 2.7.1 Hall effect

The Hall effect phenomenon creates an induced lateral potential across a semiconductor perpendicular to the direction of charge carrier motion and magnetic field due to Lorentz's force. Figure 2.7 displays a schematic of the principle of the Hall effect phenomena. The current passes from left to right, the same direction of the hole drift motion in the P-type semiconductor, while the opposite direction for electrons in the n-type semiconductor. The magnetic field is applied perpendicularly onto the specimen surface, so induced force deflects charge carriers in the lateral direction, according to Lorentz's Law (Hall 1879).

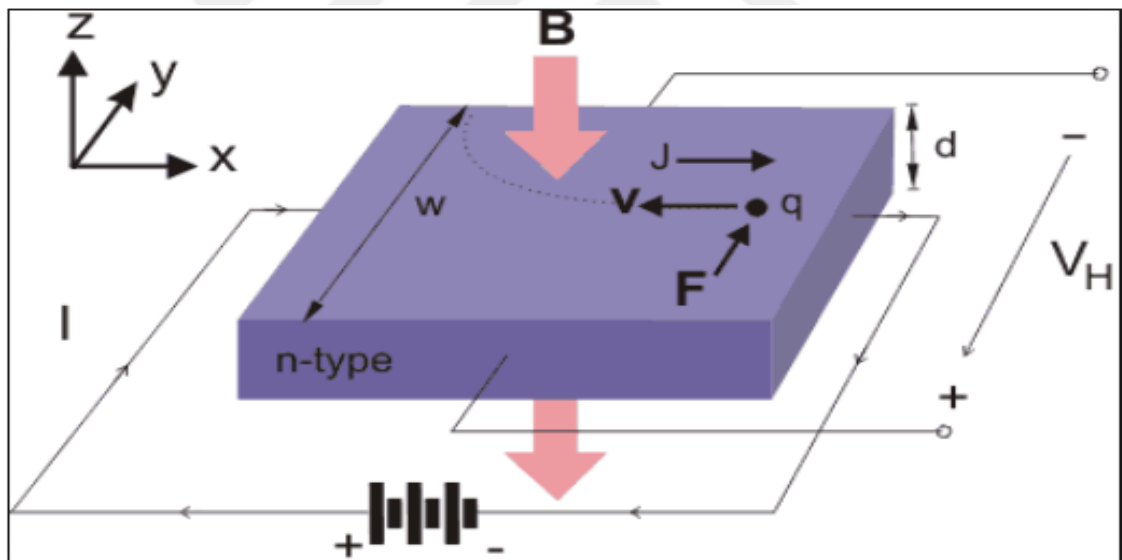


**Figure 2.7** Schematic of Hall Effect (Rai and Raj 2004)

Hall effect coefficient ( $R_H$ ) is calculated from the slope of the linear relation between the induced Hall voltage ( $V_H$ ) against the applied current ( $I_H$ ). The sign of  $R_H$  indicates the type of majority charge carriers. The Hall coefficient ( $R_H$ ) is determined according to Equation (2.7) (Rai and Raj 2004).

$$R_H = \frac{V_H}{I} \cdot \frac{t}{B} \quad (2.7)$$

The concentration of charge carriers ( $n_H$ ) is determined according to its relation with the  $R_H$  Equation (2.7) (Lindberg 1952).

$$n_H = \frac{1}{|R_H| \cdot e} \quad (2.8)$$

and the mobility of the dominant charge carriers ( $\mu_H$ ) is determined according to Equation (2.9)

$$\mu_H = \sigma |R_H| \quad (2.9)$$

## 2.8 Solar Cells

The source of solar energy is nuclear fusion, which takes place in the sun's interior at high temperatures and pressures. By joining together tiny nuclei like hydrogen, deuterium, and alpha atoms to form a new nucleus, the energy gained from the nuclei's mass loss is converted into solar energy. A solar cell is a particular kind of electrical appliance that converts light energy directly into direct current (dc) power using the photovoltaic effect (First, they form an inner electric field in the junction after diffusion processes and second create electron-hole pairs near the junction under illumination intensity). A substance that can absorb photons from the sun is needed for the conversion process. After that, an electron must be raised to a condition with a higher energy level and then flow to an external circuit. A simple solar cell structure is shown in Fig.2.8 (a) and a solar panel configuration in Fig.2.8(b), respectively. As can be seen in Fig. 2.8(a), solar cells are usually coated with anti-reflective material so that they absorb the maximum amount of radiation possible or decrease the amount of reflective photons from the rectifier front contact. A module is created by connecting solar or photovoltaic (PV) cells in series, and modules are subsequently joined in parallel-series arrangements to create arrays. To produce an additive voltage output when connecting cells or modules in series, they must have the same current rating; similarly, when connected in parallel to produce bigger currents, they must have the same voltage rating. In an ideal solar cell, a current source and a diode would be connected in parallel. But, in practice, the situation is very different, so an additional  $R_{sh}$  and  $R_s$  component is added to the model as shown in the following analogous solar cell circuit (Fig. 2.9

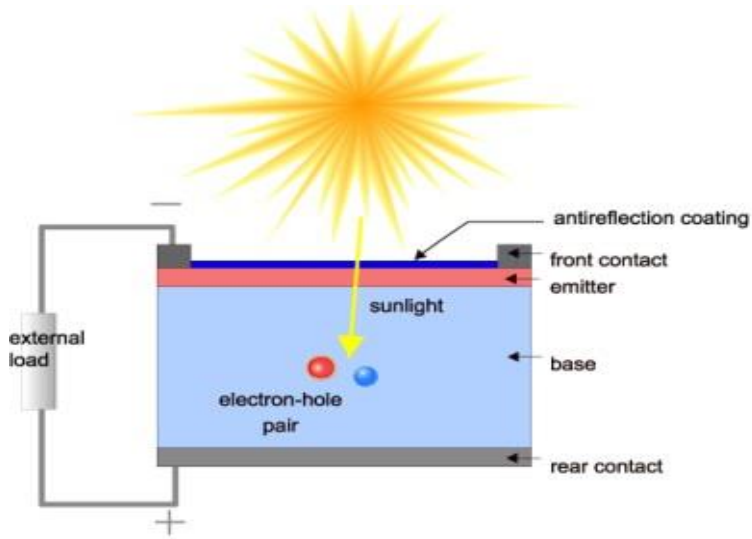


Figure 2.8 (a) Simple solar cell structure.

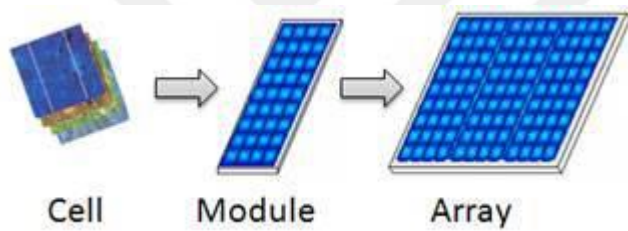


Figure 2.8 (b) Solar panel configuration.

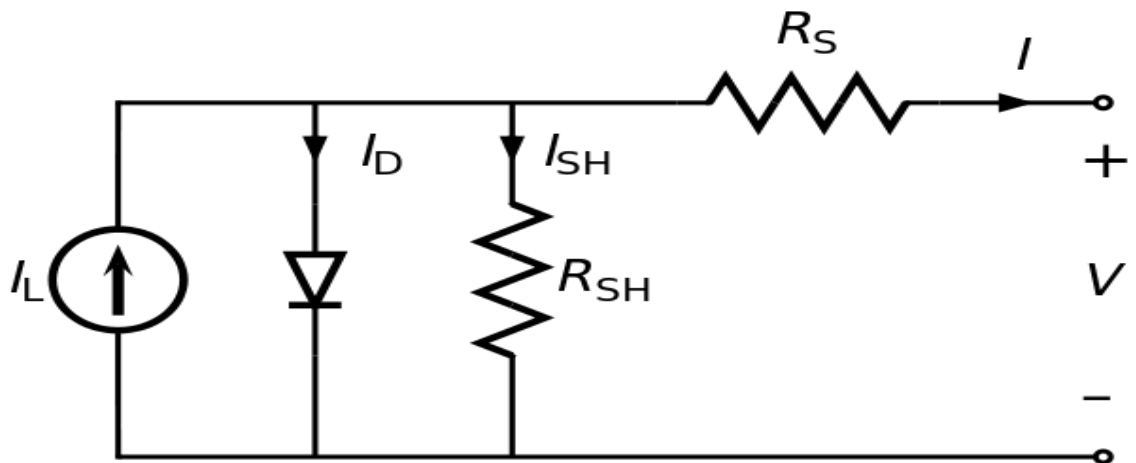


Figure 2.9 Equivalent circuit of a solar cell.

### 2.8.1 Fundamental requirements for solar cell

According to S.Gurumurthy in 1999, a solar cell must meet the following three criteria before it may be used to power an external device(Gurumurthy *et al.* 1999):

First, the cell needs space for extra electron-hole pairs to form when light is absorbed.

Two, the photo-generated carriers can be extracted by a specific process.

Third, enough time must elapse for the photo-generated carriers to be isolated. Particularly, the lifetime of the carriers must be quite long.

The first criteria is met by a base that is thick enough to surpass the absorption length or by some other light-trapping method.

A p-n junction and its accompanying intrinsic field can satisfy the second criterion. The electric field of the depletion area sweeps away the surplus electrons and holes next to the junction on the p and n sides, respectively. However, most of the light in a solar cell is absorbed in its bottom since its connection is so close to the surface. As a result, most of the free charge is made up of electrons from the base.

Finally, using materials with moderate doping and a small number of crystallographic defects leads to a longer diffusion path for electrons. It is preferable to have more doping in the base to get higher open circuit voltages (described in the following section). The reason for this is increased doping densities. A stronger gradient for the different carriers is made possible by the solid field that is generated intrinsically. Doping, on the other hand, shortens the lifetime of the carriers. Therefore, a compromise is typically struck between a larger built-in field and a longer bulk lifetime for maximum performance.

To this end, solar cells have a thick base to maximize light absorption, resulting in an

abundance of electrons that eventually make their way to the depletion area. They are carried into the emitter by the field, where they make up the vast majority of carriers and experience almost no concentration gradient. However, the Coulomb force causes the electrons to repel each other, which removes them at the front contact of the cell. Instead of using the cell's internal voltage to create a voltage differential in the external circuit, this picture used up the available charge. The emitter's extra holes act like the collector's surplus electrons.

### 2.8.2 Parameters of a solar cell

Solar cells can be described using many different metrics. Below is a quick discussion of some of these factors and how they impact the device's performance.

Figure 2.8 depicts a solar cell's I-V properties in the dark and with light. The area of interest for solar cells is the fourth quadrant, where the product of voltage and current is harmful and indicates that the cell produces electricity. The short circuit current, abbreviated as  $I_{sc}$ , is one of the parameters and is the current that flows through the circuit when the load is reduced.

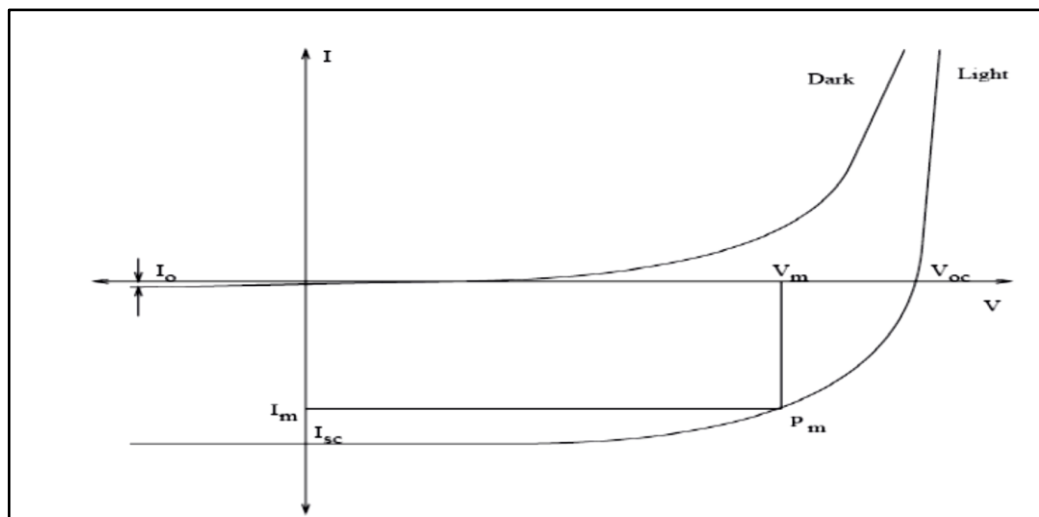


**Figure 2.8** Solar cell's dark and illuminated I-V curves

$I_0$  and  $A_0$  give important information about a device's primary current transfer mechanism. There are several techniques for getting these parameters, however the most reliable approach is determining them using dark I-V curves. The  $A_0$  is given by the slope of the I-V curve, whereas the  $I_0$  is given by the y-intercept. They are frequently considered together since these metrics have a high degree of association. By reducing  $I_0$ ,  $V_{oc}$  may be maximized by raising the voltage needed for the dark current to equal the current provided by light.  $V_{oc}$  is reduced and device fill factors are increased when  $A_0$  is made smaller. Further research is needed to fully understand the nuances of the  $A_0$  vs.  $I_0$  debate and how these properties affect cell behavior (Kohl 1998).

$I_s$  and  $V_{oc}$  are the short circuit current and open circuit voltage, respectively, while  $I_m$  and  $V_m$  are the maximum power point current and voltage. This is the maximum power that the gadget can produce.

A (Si) For detecting the growth of the bitmap layer and managing chemical dissolution in HF acid, silicon is virtually completely ineffective when anodically biased (Sun *et al.* 2019).

Silicon anodization triggers a chain reaction leading to either heat production or a photogenerated process. Before discovering the supply response limits of the electrode, the bias hole is applied to the silicon/solution interface, which may elicit a reaction. The condition does not change for current densities (J) less than the critical current density (Lehmann and Föll 1990).

If a hole ( $H^+$ ) reaches the surface, nuclear assault by fluoride ions (F) can occur, resulting in the formation of a Si-F bond.

Another generation of F ions may be formed under the influence of an  $H_2$  molecule and an electron injection to bulk silicon (step 2) due to the effect of the F-bonded polarizing. In steps 4 and 5, HF further weakens the bonds between silicon atoms and hydrogen

molecules, allowing the silicon atoms to remain attack connected to the hydrogen atoms despite the polarization brought on by the Si-F. (step 5).

Removing a silicon atom from the ground state maintains a smaller nuclear volume. As a result of the shift in the field's spreading geometry, transmission will take place at this ideally perforated location (Kohl 1998).

## 2.9 Zinc Oxide

Wide band gap, II-VI compound with a wurtzite-type structure, zinc oxide (ZnO). It has a 3.37 eV band gap. An n-type semiconductor with good conductivity is pure ZnO. Cationic substitution using a trivalent element like Al, Ga, or In can increase ZnO's conductivity and carrier concentration. ZnO is widely utilized in optoelectronic devices, sensors, spintronics, and photovoltaic applications because of its unique qualities, including low resistivity, broad bandgap and great optical transparency Figure 2.9.

Zinc oxide thin film has a high transmittance at 800-1100 nm and low resistivity, potentially replacing ITO film. Annealing processes can enhance thin film properties by increasing crystallization and reducing defects. On the other side, doping or composing with other materials is an effective way to attain high properties of ZnO film Table 2.1 (Chen 2018).

**Table 2.1** Some physical properties of ZnO (Ngom *et al.* 2009)

Name	Property
Molecular formula	ZnO
Appearance	White Solid
Molar Mass	81.408g/mol
Boiling Point	2633 K
Density	5.606 g/m <sup>3</sup>
Band Gap	3.3eV
Refractive index	2.0041
Water Solubility	0.16 mg/100 mL

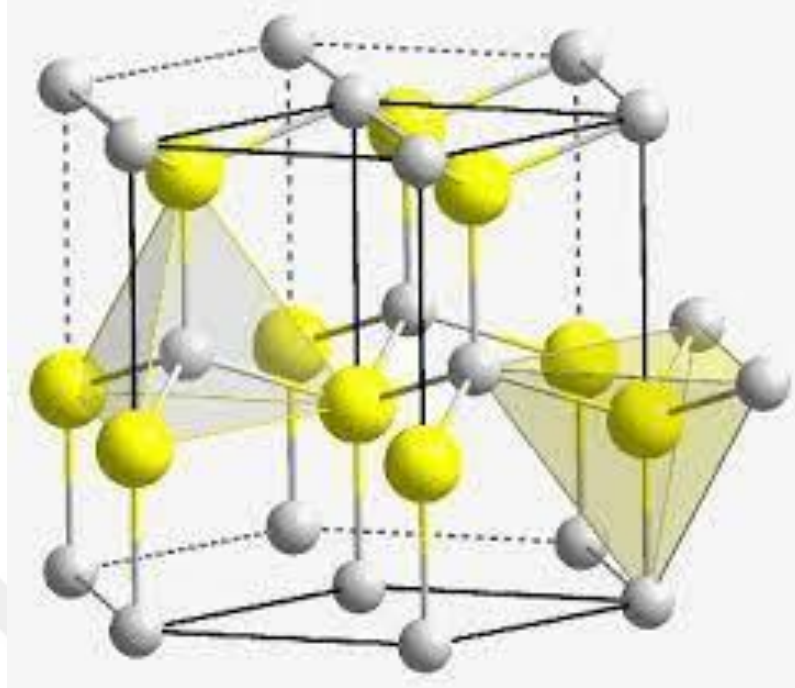


**Figure 2.9** Zinc oxide structure

### **2.10 Indium Oxide**

In contrast to indium oxide, which is insoluble in both water and acids, amorphous indium oxide is soluble in acids but not in water. Two distinct crystalline phases may be observed: cubic (bixbite type) and rhombohedral (corundum type). Both phases have a same 3 eV bandgap. Parameters of the cubic phase are detailed in the accompanying infobox (Marezio 1966).

The rhombohedral phase is formed using non-equilibrium growth techniques or at high temperatures and pressures. The rhombohedral phase is formed using non-equilibrium growth techniques or at high temperatures and pressures. It has a space group R3c No. 167,  $a=0.5487$  nm,  $b=0.5487$  nm,  $c=1.4510$  nm,  $Z=6$  and calculated density  $7.31$  g/cm<sup>3</sup> Figure 2.10 (Walsh *et al.* 2008).

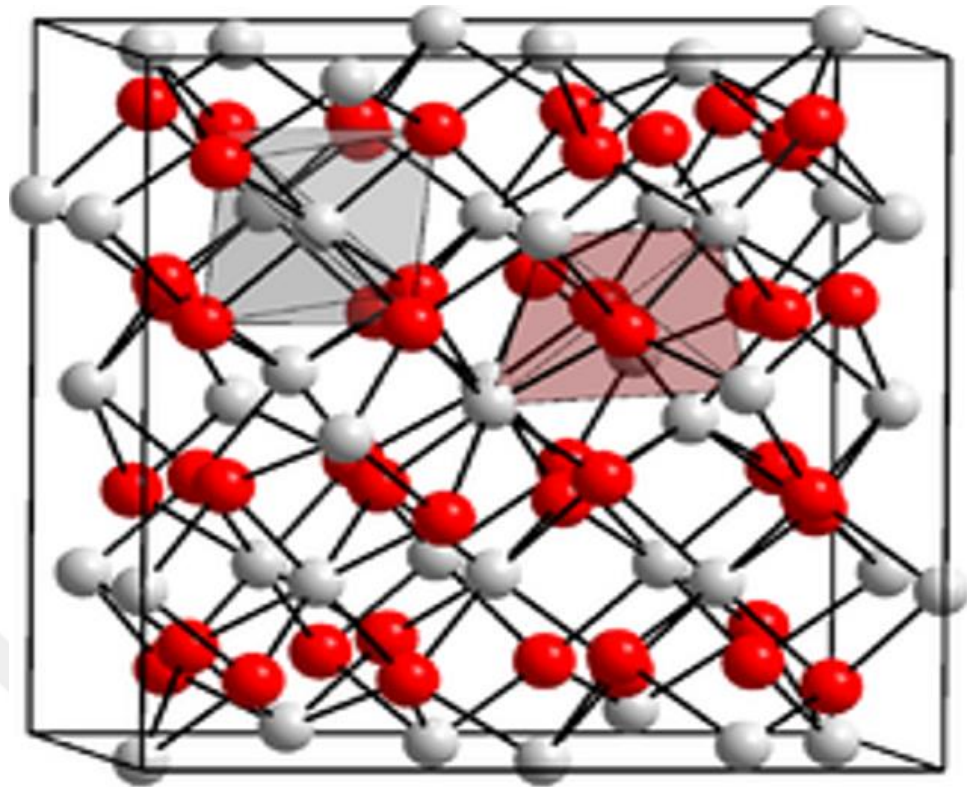


**Figure 2.10** Indium oxide crystal structure

A thin indium oxide coating may be made by sputtering indium targets in an argon/oxygen atmosphere. Diffusion barriers in semiconductors may be constructed using these films (Kiriakidis *et al.* 2001).

Mono-crystalline indium oxide nanowires may be fabricated using laser ablation, enabling diameter tuning down to 10 nm. They were utilized to develop field effect transistors, and redox protein sensors based on indium oxide nanowires are very sensitive and accurate (Khashan and Mahdi 2017).

Another technique for making nanowires is the sol-gel approach. An example of a semiconductor material is indium oxide, producing heterojunctions with materials such as p-InP, n-GaAs, and n-Si Table 2.2. A useful technique for creating the photovoltaic device is to deposit an  $\text{In}_2\text{O}_3$  layer from an indium trichloride solution onto a silicon substrate (Lu *et al.* 2006).

**Table 2.2** Some physical properties of indium oxide

Name	Property
Molecular formula	In <sub>2</sub> O <sub>3</sub>
Molar Mass	277.64 g/mol
Appearance	Yellowish-green odorless crystals
Density	7.179g/cm <sup>3</sup>
Melting Point	2180K
Band Gap	3eV
Water Solubility	Insoluble
Crystal Structure	Cubic

### 2.11 Fundamental Properties of Tungsten Oxide

One of the most intriguing materials, WO<sub>3</sub> exhibits a wide range of new qualities that make it particularly valuable for sophisticated technological applications when forming thin films. It demonstrates structural changes and sub-stoichiometric phase transitions, which have drawn the interest of academics in recent years to consider its possible use in science and technology, particularly in microelectronics and display systems (Szkoda *et al.* 2020).

The morphology and structural organization of a material have a significant impact on its physical qualities. The film quality and material production costs of various preparation techniques vary depending on the application. Despite being a known promising material for electrochromic devices, tungsten oxide was not widely used due to the rapid advancements in displays using liquid crystals. Currently, sunglasses, rear-view mirrors for cars, windows for automobile glass, and building windows all employ tungsten oxide films (Akkurt *et al.* 2020).

With encouraging findings, several researchers have constructed and tested complete electrochromic systems. Some physical properties belong to WO<sub>3</sub>, as is played in Table 2.3.

**Table 2.3** Some physical properties of WO<sub>3</sub> (Ge *et al.* 2018)

Name	Property
Symbol, number	<sup>74</sup> WO <sub>3</sub>
Element category	Transition metal
Crystal structure	Monoclinic
Molar mass	231.84gm/mol
Density	7.16 gm/cm <sup>3</sup>
Melting point	1746 K
Appearance	yellow powder
Boiling point	1970 K
Molecular weight	231.84 g/mol

The molecular structures related to the supported transition metal oxide catalyst within dry conditions. Notably, it is verified how many terminal M=O (metal-oxide) bonds existed in surface molecular entities. Also, the transition metal oxides might likely exist as di-, mono- or trioxo species, while the metal oxides were studied for gas detection applications (Jiang *et al.* 2018). This is due to the way they operate, which involves differences in surface electrical conductivity when a gaseous environment is present. Through the adsorption of gaseous species from surrounding atmospheres, such induced electrical conductivity was altered. At the same time, metal oxide causes the dissociation of the gas into complexes on the surface or charged ions, which leads to electron transfer. Such property was utilized to detect toxic and combustible gases. In addition, such materials' electrical properties depend on chemical compositions regarding metal-oxide surface and nature as well as the work function behaviour. Whereas the adsorption coefficient, the electron donor/acceptor characteristics of testing gas, the nature of surface sites, subsequent desorption of gases, and the surface reactions were the significant features determining the performances of metal oxide gas sensors. In contrast, the surface interactions between solids and gas primarily occur. Therefore, the number of atoms that reside in the grain boundaries (GB) and the interface is significant in controlling the characteristics of such sensors.

Typically, such gases induce resistance increase on the n-type semiconductor oxides. Also, increasing resistance might correspond to the surface process and indicate capturing the free electrons from the semiconductor's conduction band via adsorbed species (Diwald and Hartmann 2021).

It is typically specified that the air-conductance behaviour and the metal oxide samples represent the impact of surface reactions involving electron exchange with oxide, majorly the ones involving water vapour and atmospheric oxygen. In contrast, the mechanism of the sensing in the metal oxide sensors is associated with the species' ion sorption on the sample surfaces. The primary significant ions sorbed species operating in the ambient air are water and oxygen. Majorly, the sensing mechanism is handled via the fact that oxygen vacancies on oxide surfaces were chemically and electrically active. Concerning such conditions, there are 2 types of sensing responses that were indicated.

### 3. EXPERIMENTAL WORK AND PROCEDURE

This chapter describes the materials and the procedure for sample preparation, substrate preparation, thin film deposition technique, and characterization of the prepared thin films. The characterization techniques comprise X-ray diffraction (XRD), Energy dispersive X-ray spectroscopy with atomic force microscopy (EDX), UV-visible absorbance, and Hall effect measurements. Finally, The characterization of the heterojunction specification. Figure 3.1 shows the scheme for experimental work.

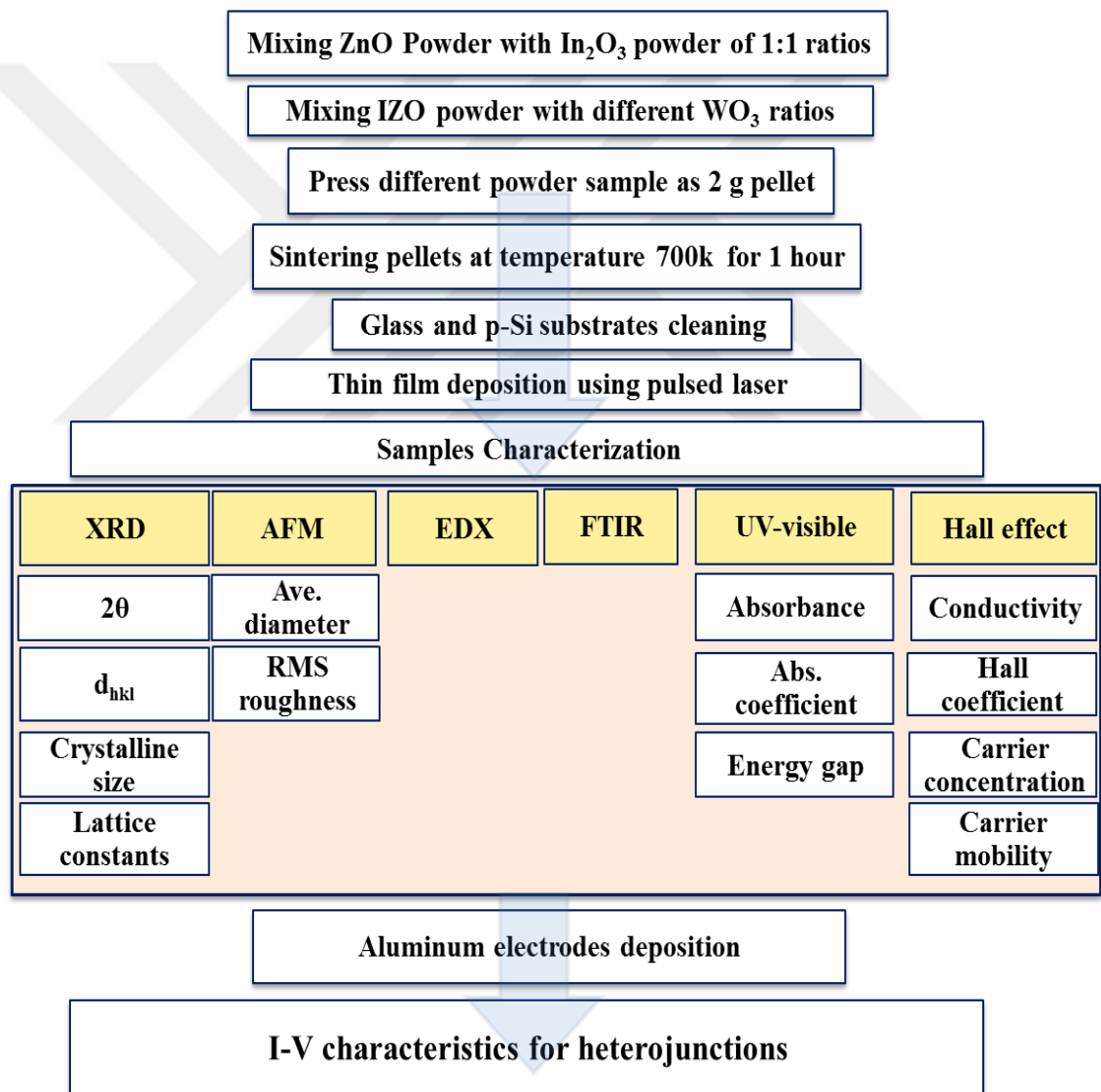


**Figure 3.1** Scheme for experimental work

### 3.1 Materials

The started materials for our work to prepare ZnO, IZO, and IZO: WO<sub>3</sub> at different percentages of WO<sub>3</sub> thin film prepared by pulsed laser deposition, their properties, sources, and purity are listed in Table 3.1.

**Table 3.1** Chemical materials

<b>Zinc (II) Oxide</b>	
<b>Chemical formula</b>	ZnO
<b>Appearance</b>	White powder
<b>Molecular weight</b>	81.37 g/mole
<b>Density</b>	5.60 g/cm <sup>3</sup>
<b>Melting Point</b>	1975°C
<b>Boiling point</b>	2360°C
<b>Purity</b>	99.999%
<b>Company</b>	BDH chemical Ltd Poole England
<b>Indium (III) Oxide</b>	
<b>Chemical formula</b>	In <sub>2</sub> O <sub>3</sub>
<b>Appearance</b>	White powder
<b>Molecular weight</b>	277.64 g/mole
<b>Density</b>	7.18 g/cm <sup>3</sup>
<b>Boiling point</b>	850°C
<b>Purity</b>	99.99 %
<b>Company</b>	BDH chemical Ltd Poole England
<b>Tungsten Oxide</b>	
<b>Chemical formula</b>	WO <sub>3</sub>
<b>Appearance</b>	Liquid
<b>Molecular weight</b>	231.84
<b>Density</b>	0.9 g/mL
<b>Boiling point</b>	80°C
<b>Company</b>	American Elements

### 3.2 Pellet Samples Preparation

Pure ZnO, IZO, and IZO: WO<sub>3</sub> at different ratios of WO<sub>3</sub> powder. The preparation of the samples pure zinc oxide powder at a ratio of 5.8 with high purity (99.999%) was mixed with indium oxide at a molar ratio of 2.2. After that, the final powder was doped with tungsten oxide in three different contents (0.05, 0.1, and 0.15 Wt ratio).

Then the powder samples were mixed using a gate Mortar for half an hour and pressed into pellets with a diameter of 1 cm and thickness of 0.2 cm using a hydraulic press, using a stainless steel mould, as shown in Figure 3.2, at a pressure of up to 5 tons for ten minutes period. A thermal oven sintered the pellets at a temperature of 973 K for one hour; then, the pellets were left cool to room temperature.

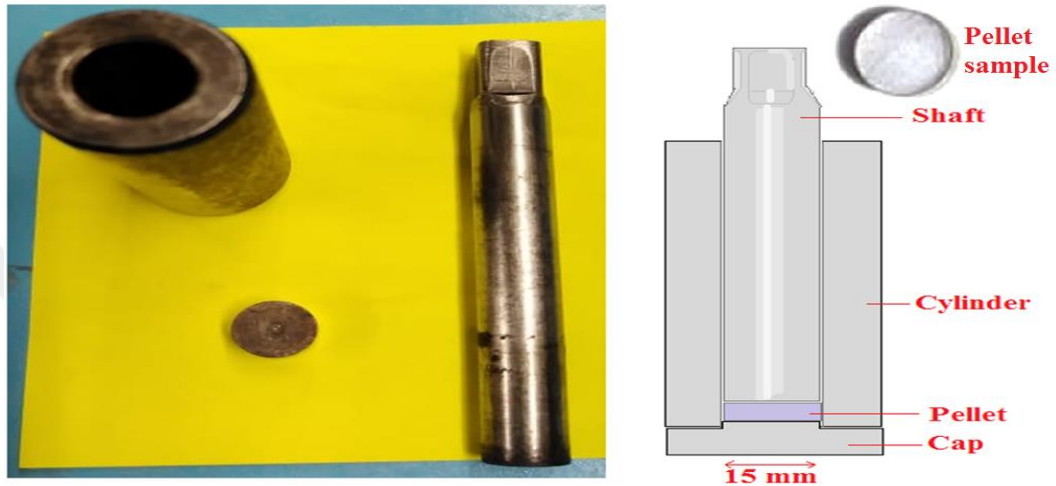


**Figure 3.2** The stainless steel mould for pressing the pellet targets

### 3.3 Substrate Preparation

The type and purity of the substrate highly affect the properties of the deposited thin films. At the same time, the purity and cleaning of the deposition substrates affect the prepared films' adhesion. Two types of substrates were used in this work: glass and silicon wafers. Glass slides are used to deposition samples to study their structural, metrological, optical, and electrical characteristics, while p-type silicon wafer substrates with a crystalline direction (100) and low electrical resistivity ( $4^{-10}\Omega.cm$ ) are used to fabricate the photovoltaic device.

#### 3.3.1 Glass substrate cleaning procedure

Glass substrates of dimensions  $(2.5 \times 2.5) \text{ cm}^2$  were used to deposit ZnO,  $\text{In}_2\text{O}_3:\text{ZnO}$  (IZO), and  $\text{IZO}:\text{WO}_3$  at different ratios of thin film PLD. The surfaces used must be

free from contamination, such as grease, dust, etc. The substrates are cleaned in several steps, as follows:

- They were cleaned with a detergent with water to eliminate any oil or dust sticking to the surface using running water for 15 minutes.
- They were washed ultrasonically for 15 minutes in distilled water.
- The washing process is repeated for 15 minutes in pure alcohol to remove contaminants.
- The substrates are finally dried using blowing air.

### **3.4 Silicon Substrate**

For solar cell production Boron doped, p type, one/double side polished, 2" wafers with 1-5  $\Omega\text{cm}$  resistivity and 300 $\mu\text{m}$  thickness has been used. Wafers first went through an ultrasonic acetone, alcohol, deionize (DI) water with 18 M. $\Omega\text{cm}$  resistivity cleaning and a dilute HF dip to remove oxide formed on the surface. Then wafers went through a texturing process in a 3% KOH solution at 75°C for 45 minutes to form micro pyramid on the surface for light trapping. To remove metallic contamination, an HF:HCl cleaning was performed which is followed by RCA2 cleaning and another HF:HCl dip. After rinsing and drying, the p-Si wafers were dried with dry nitrogen ( $\text{N}_2$ ) gas. After cleaning processes, high-pure Al was evaporated onto p-Si wafer and then annealed at 500°C to get low resistivity an ohmic contact

#### **3.4.1 Photochemical etching**

Photochemical etching provides a porous silicon layer. This process is carried out by using a common light source. Figure 3.3 depicts the setup for the photochemical etching procedure. A Philips halogen lamp light of 120 W and diluted etching hydrofluoric acid in a container make up the arrangement. The distance from the light to the sample was 15 cm. The porous silicon was created on the sample's lighted side. A photo etching irradiation duration of 10 minutes was used. To prevent the formation of an oxide layer

on the Si wafer, the samples were rinsed with ethanol after the photochemical etching procedure and kept in a glass container filled with Methanol.

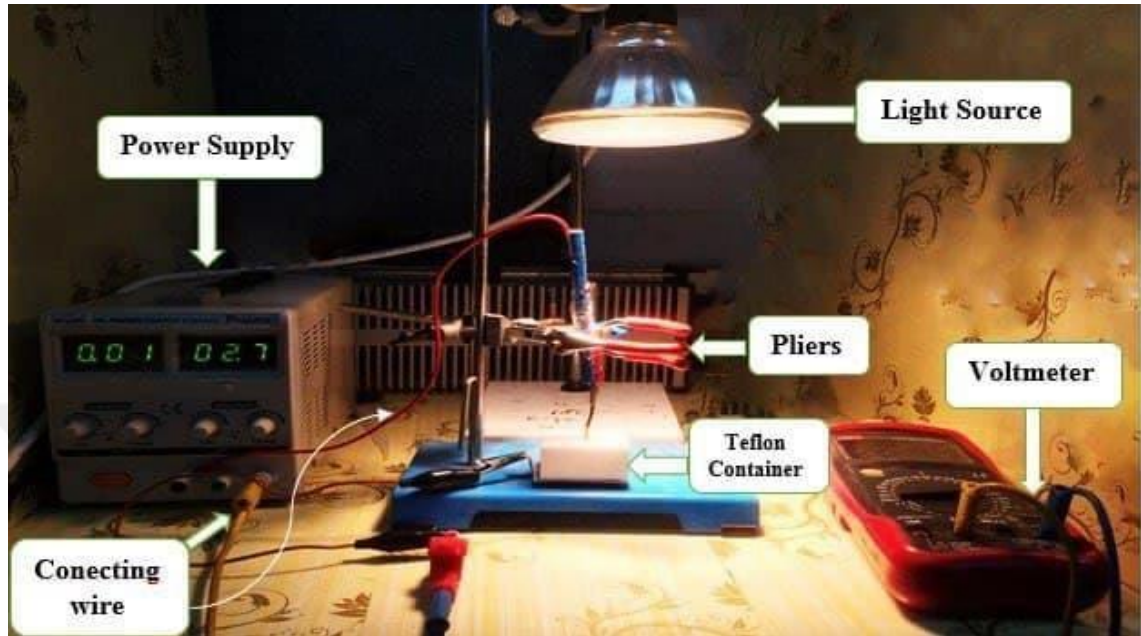


**Figure 3.3** Photograph of the setup of the photochemical etching process

### 3.5 Thin Films Preparation

ZnO, IZO, and IZO: WO<sub>3</sub> at different percentages of WO<sub>3</sub> thin film prepared by PLD technique under vacuum of 10<sup>-2</sup> bar pressure. The vacuum chamber made of Pyrex glass of cylindrical shape has a 25 cm diameter and 30 cm height, as shown in Figure 3.4. The chamber is vacuumed using a double-stage rotary pump. The target is fixed horizontally at 2 cm above the target. Nd: YAG pulsed laser is focused on the pellet sample, with an angle of 45° with its surface, through the glass wall of the chamber. Many pulses were used to prepare thin films at a fixed energy.

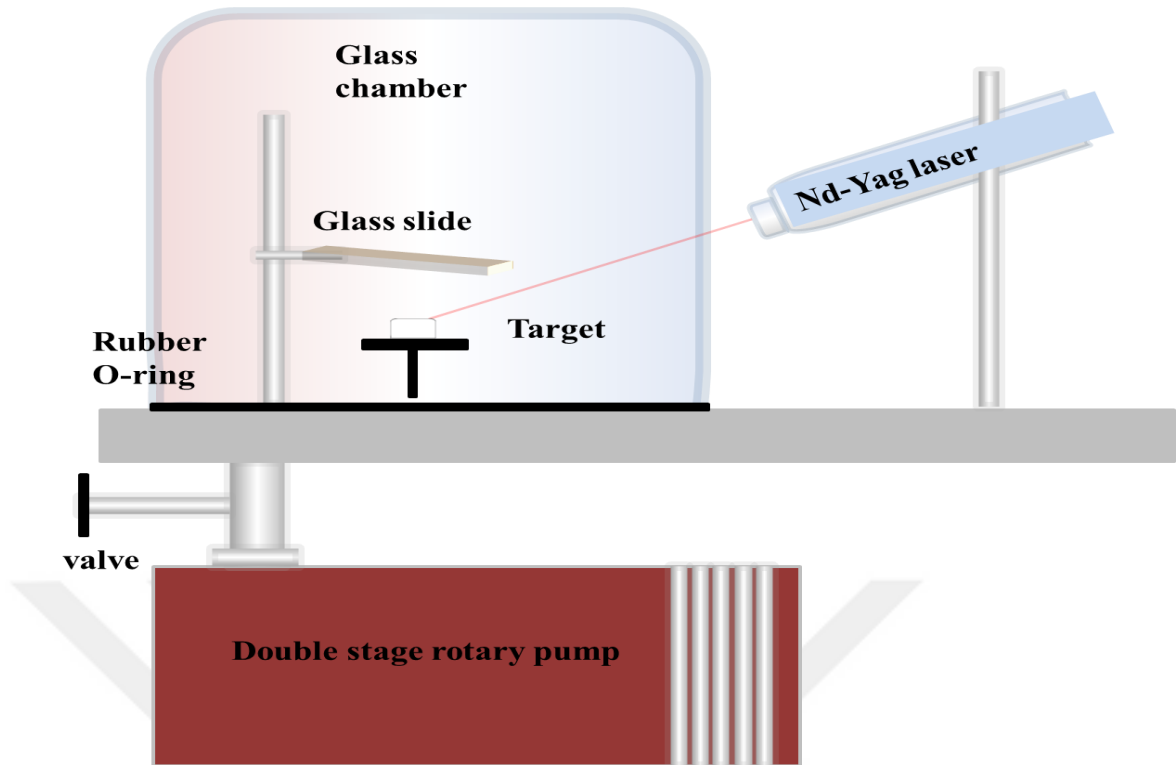


**Figure 3.4** Scheme of the PLD setup

### 3.5.1 The laser source

The laser source of Nd: YAG laser (DIAMOND-288) was used in the PLD system of Q-switched laser using the primary generation of wavelength 1064 nm. Its energy density was 0.8-1.8 J/cm<sup>2</sup>. Its pulse duration was 10 ns and 6 Hz repetition frequency. The pulse energy can be increased in steps of 20 mJ. The laser spot size, repetition frequency, and pulse number are controllable. Thin films were deposited at a constant pulse laser energy of 500 MJ using several 200 pulses.

### 3.6 Thin Films Characterization

The characterization measurements are used to investigate properties which include: the films thicknesses (using a reflectance probe), structural properties optical characteristics (using UV-visible absorption spectrometer), surface morphology (using atomic force microscopy), electrical properties, and X-ray diffraction (using Hall Effect Measurements).

### 3.6.1 The thickness of thin films

The thin film thickness was determined using the reflectance probe (SR300 Angstrom Sun Technologies) displayed in Figure 3.5 at a halogen lamp's wavelength range (400 to 1100) nm. The light beam through an optical fibre falls perpendicularly to the sample, and a sensor measures the refracted light. The thickness of thin films is determined using the attached software. The sample thickness was fixed between 200 nm to 10 nm.

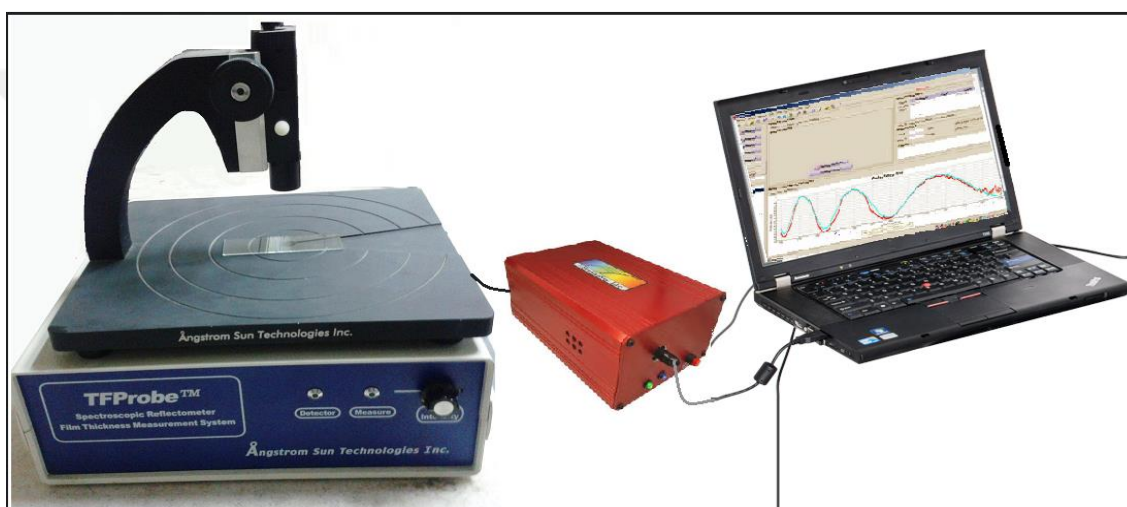


**Figure 3.5** Optical thickness measurement

### 3.6.2 X-ray diffraction (XRD)

The structural properties for ZnO, IZO, and IZO: WO<sub>3</sub> thin films prepared by PLD at different doping concentrations were examined by XRD instrument (Shimadzu XRD 6000) with X-ray tube of Cu (K<sub>α</sub>) radiation of 1.5406 Å wavelength, using 40 kV voltage power supply and 30.0 mA current. The scanning angle was within the range of (2θ=20-80 degrees) with a speed of 5.00 (degree/min).

### **3.6.3 Atomic force microscopy (AFM)**

ZnO, IZO, and IZO: WO<sub>3</sub> thin films were produced by PLD, and their surface morphology was studied using an atomic force microscope (AFM) to examine average particle diameter and surface roughness. Tapping mode AFM models were used for the analysis (AA3000 Scanning Probe Angstrom Advance Inc).

### **3.6.4 UV-visible absorbance**

The optical properties of the prepared thin films on glass slides by PLD technique at room temperature were tested by UV-visible absorption. The optical characteristics of the deposited thin films are determined by the deposition parameters, film thickness, surface morphology, and doping concentration. The measurements were taken using a UV-Visible SP-8001 spectrophotometer with a wavelength range of (300-1100) nm. To cover the complete spectrum, the spectrometer has two light sources (Deuterium and Tungsten). A computer connected to the spectrometer calculates the output transmittance and absorbance.

### **3.6.5 Hall effect measurements**

Hall Effect is an important technique to examine the electrical properties of semiconductors' thin films. The result gives evidence on semiconductor type, charge carrier concentration, and mobility.

Four Aluminum electrodes are deposited on its surface. Charge carriers are deflected in one direction when a magnetic field ( $B=0.550$  Tesla) is applied perpendicular to the electric field. Hence, we apply a voltage across the sample, denoted by  $V_H$ . The sign of the Hall coefficient determines the dominant carrier type. Hall effect investigations were performed using Ecopia HMS-3000 instrument. The Hall coefficient ( $R_H$ ) was calculated using the change of the applied current with the generated inductive voltages.

### 3.7 Heterojunction Fabrication

After the cleaning process of the silicon substrate and creating a porous layer by electrochemical etching, as explained previously, thin films of ZnO and IZO: WO<sub>3</sub> thin films prepared by PLD at different doping concentrations above this layer. Aluminium electrodes are deposited as wholly covered on the rear surface of a silicon wafer and as mesh shape on the front surface using the appropriate masks by thermal evaporation under vacuum. Thin and insulated wires were connected with aluminium electrodes using a silver paste, as shown in Figure 3.6.

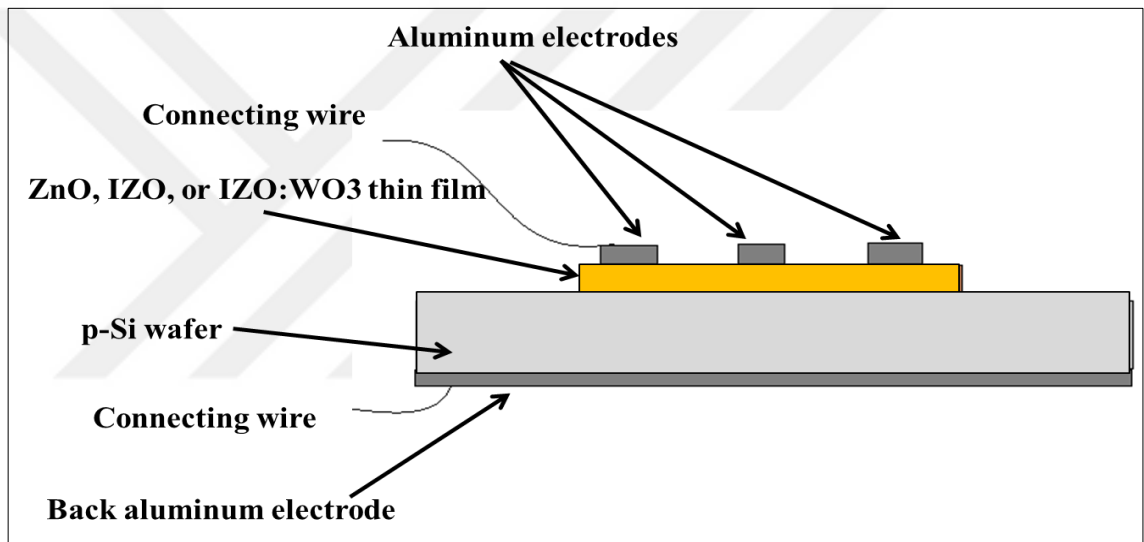


**Figure 3.6** Schematic diagram for the prepared photovoltaic device

#### 3.7.1 Mask preparation

Unique masks for the Hall effect and solar cell device have been put on the deposited thin films to deposit aluminium as ohmic contact using a thermal evaporation system under vacuum with Tungsten boats under  $10^{-5}$  bar pressure. The two types of masks are shown in Figure 3.7 and Figure 3.8.

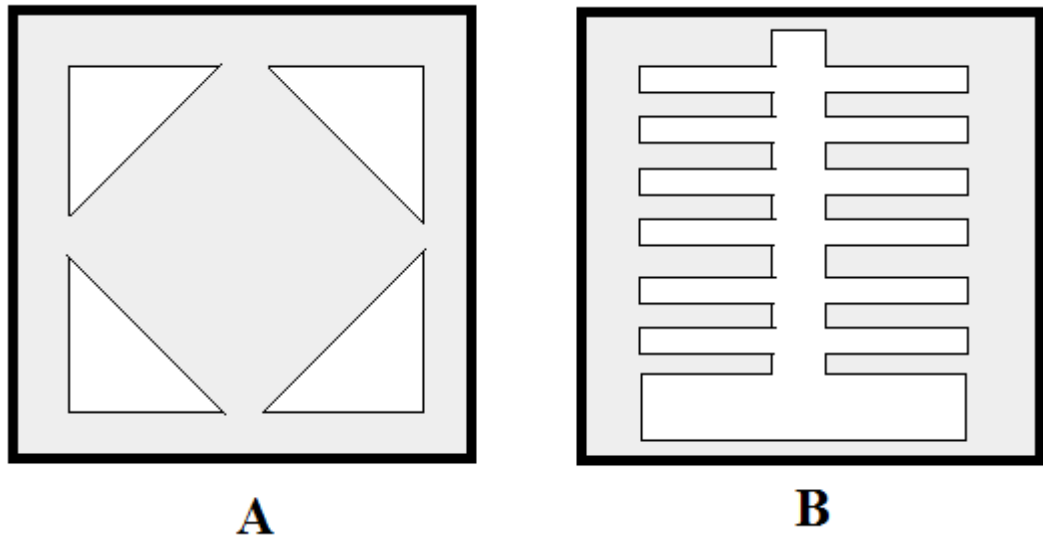


**Figure 3.7** On the films for (A) the Hall effect electrode and (B) the solar cell mesh electrode, the white masks denote the aluminium electrodes

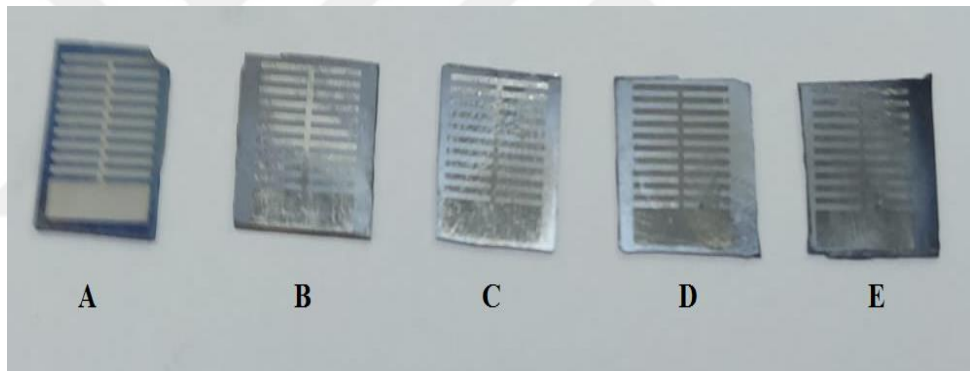


**Figure 3.8** IZO:WO<sub>3</sub>/p-Si heterojunction samples at different WO<sub>3</sub> contents (A) 0, (B) 10%, (C) 20%, (D) 30%, and (E) 40%

### 3.8 The I-V Characteristics for the Heterojunctions

The I-V features for the combined solar cell samples based on Al/IZO/p-Si/Al and Al/IZO: WO<sub>3</sub>/p-Si/Al heterojunctions illuminated by a halogen light 100 mW/cm<sup>2</sup> light intensity, by using a digital electrometer, voltmeter, and D.C. power supply. The bias voltage was varied over the range of -0.5 to 1.5 Volt. The voltage was adjusted by fine-tuning the applied potential and monitored by the voltmeter, while the current was recorded using an Amperemeter. Figure 3.9 shows a schematic diagram of a circuit for I-V characteristics measurements.

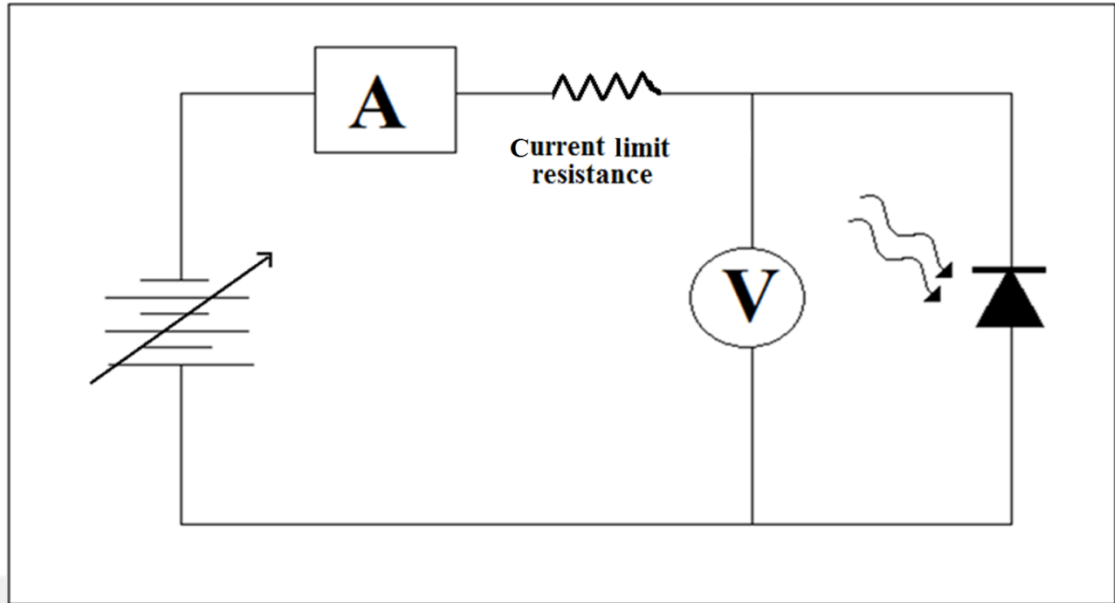


**Figure 3.9** Schema of I-V characteristics examination circuit for the photovoltaic device

Other parameters corresponding to the heterojunction, such as the conversion efficiency, the filling factor, the short circuit current, and the open circuit voltage were determined using the I-V curves under light versus the applied voltage from -0.5 to 1.5 V.

## 4. RESULTS AND DISCUSSION

### 4.1 Introduction

The findings of the examinations of structural characteristics (by XRD), surface morphology (by AFM and SEM), and elemental analysis are included in the analysis of results and comments in this chapter (by EDX), molecular bond (by FTIR), optical properties (by UV-vis.), and electrical properties (by Hall effect) for the ZnO, In<sub>2</sub>O<sub>3</sub>:ZnO (IZO), and IZO: WO<sub>3</sub> at different percentage of WO<sub>3</sub> thin film prepared by pulsed laser deposition technique on a glass substrate.

### 4.2 Structural properties

The XRD patterns of the ZnO thin films produced on glass substrates are displayed in Figure 4.1 and Table 4.1. The Polycrystalline nature of the hexagonal ZnO structure matched with the JCPDS Card No. 96-230-0114. The diffraction lines located at 31.7976°, 34.5043°, 36.3040°, 56.6475°, and 68.0070° corresponding to the crystalline planes of (001), (002), (101), (110), and (112), respectively.

The inter-planer distances  $d_{hkl}$  was determined using Bragg's law Equation (4.1) (Dintle *et al.* 2018)

$$n\lambda = 2d_{hkl} \sin\theta \quad (4.1)$$

while the crystalline size (C.S) was calculated using to Scherrer formula, Equation (4.2) (Dintle *et al.* 2018).:

$$C.S = \frac{0.94 \lambda}{\beta \cos\theta} \quad (4.2)$$

Where  $\theta$ ,  $\lambda$ ,  $n$ , and  $\beta$  are represented by Bragg's diffraction angle, X-ray wavelength (= 0.154061 nm), the diffraction order, and the full width at half maximum (FWHM) in rad, respectively.

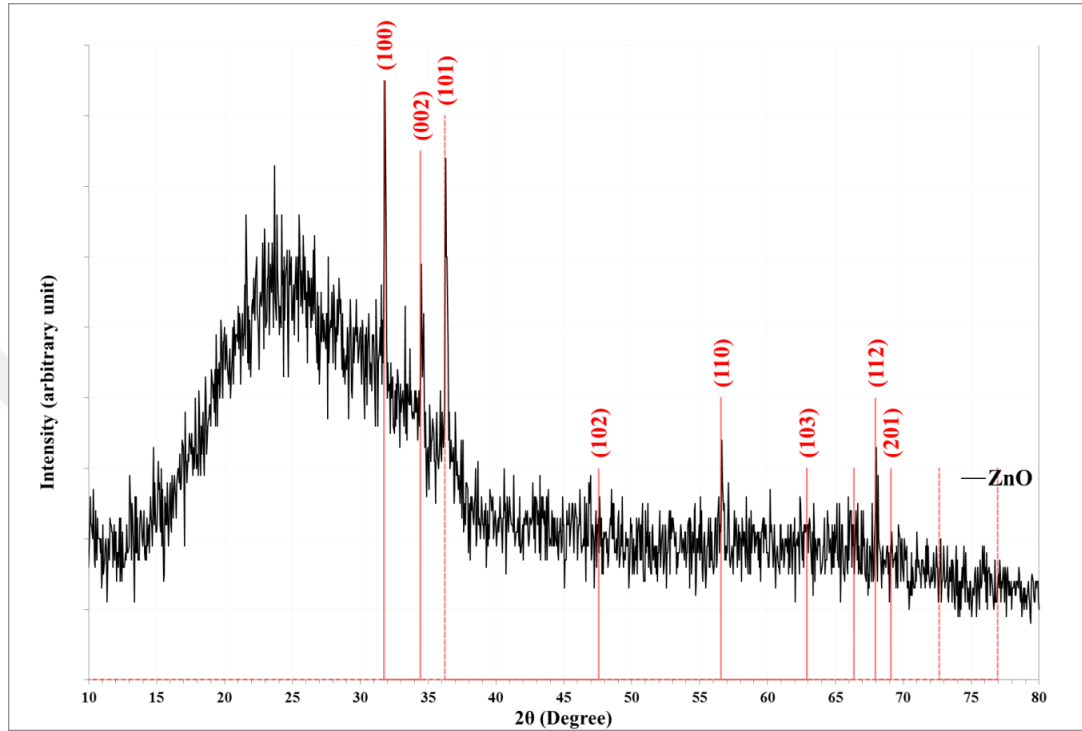


**Figure 4.1** XRD patterns for the ZnO thin films on glass slides

**Table 4.1** XRD parameter for the ZnO thin films on glass slides

2θ (Deg.)	FWHM (Deg.)	$d_{hkl}$ Exp. (Å)	C.S (nm)	hkl
31.7976	0.1440	2.8119	57.4	(100)
34.5043	0.2016000	2.5973	41.3	(002)
36.3040	0.2160	2.4726	38.7	(101)
56.6475	0.2303	1.6236	39.2	(110)
68.0070	0.2592	1.3774	37.0	(112)

Figure 4.2 and Table 4.2 illustrates the XRD patterns for thin films of pure IZO that compose different ratios of  $WO_3$  samples deposited on glass slides by the PLD technique at room temperature. All patterns appeared as polycrystalline structures. The pure IZO sample has a structure identical to the ZnO hexagonal phase of JCPDS Card No. 96-230-0114. This agrees with previous studies (Ghosh and Pandey 2019).

The doped samples with different ratios of  $\text{WO}_3$  appeared as a mixed phase of both triclinic  $\text{WO}_3$  according to the JCPDS Card No. 96-101-0619 in addition to the ZnO phase. They are increasing the  $\text{WO}_3$  content cause to increase in the intensity of peaks corresponding to the  $\text{WO}_3$  structure (Kowalkińska *et al.* 2022). The location of ZnO diffraction peaks slightly shifted with increasing the  $\text{WO}_3$  content as a result of constant strain in the lattice (Soltabayev *et al.* 2019), indicate on the diffusion of some tungsten atoms within the ZnO lattice. In addition, the broadening of the diffraction lines indicates that increasing the crystalline size directly with the  $\text{WO}_3$  content increases.

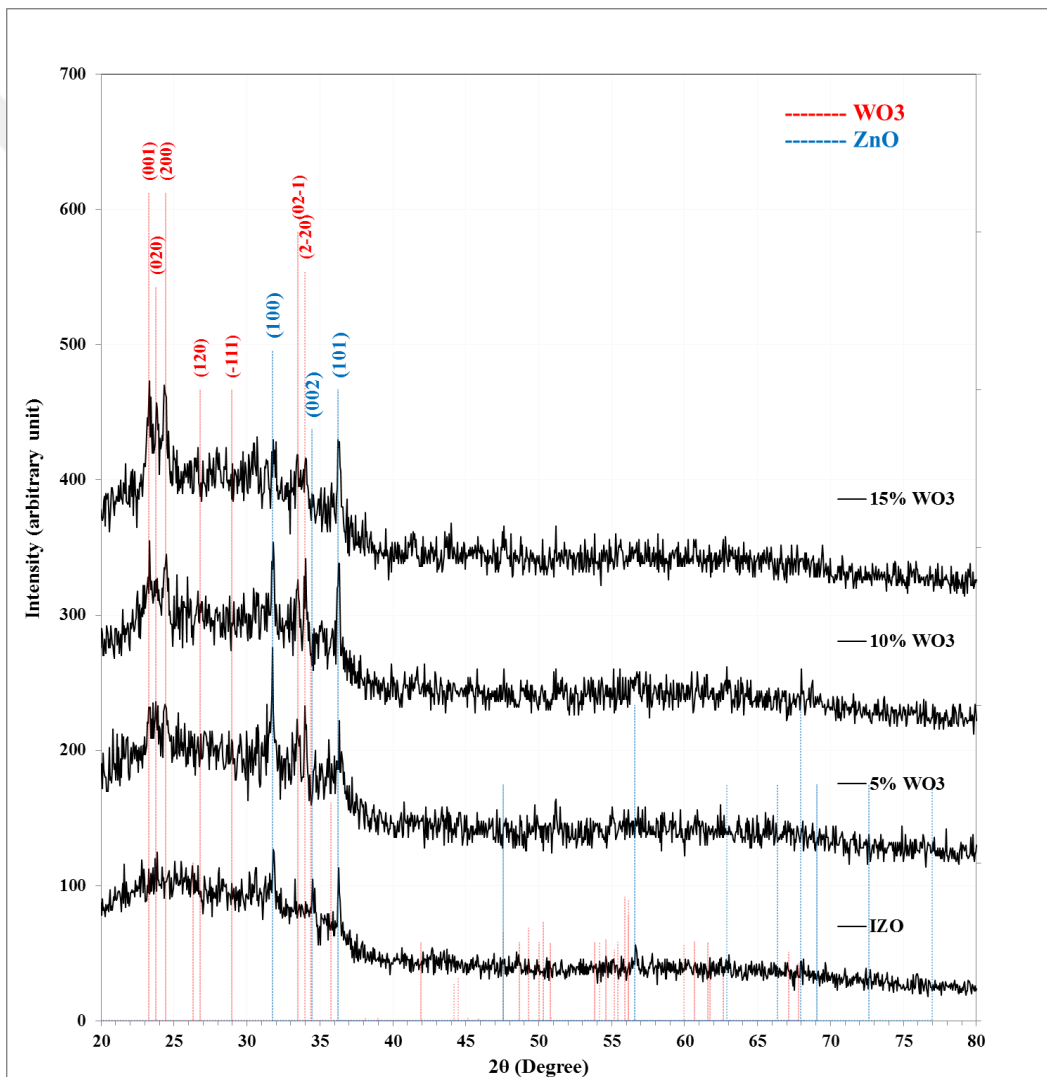


**Figure 4.2** XRD patterns for pure IZO films and that doped with different contents of  $\text{WO}_3$

**Table 4.2** XRD patterns for pure IZO films and that doped with different contents of WO<sub>3</sub>

WO <sub>3</sub> %	2θ (Deg)	FWHM (Deg)	d <sub>hkl</sub> (Å)	C.S (nm)	hkl	Phase
IZO	31.8082	0.2421	2.8110	34.1	(100)	ZnO
	34.4995	0.2608	2.5976	31.9	(002)	ZnO
	36.2968	0.2607	2.4730	32.1	(101)	ZnO
5%	23.2780	0.2607	3.8182	31.1	(001)	WO <sub>3</sub>
	24.3955	0.3539	3.6458	23.0	(200)	WO <sub>3</sub>
	31.7523	0.2980	2.8158	27.7	(100)	ZnO
	33.4565	0.3073	2.6762	27.0	(02-1)	WO <sub>3</sub>
	33.9593	0.2328	2.6377	35.7	(2-20)	WO <sub>3</sub>
	36.3619	0.2514	2.4688	33.3	(101)	ZnO
10%	23.2873	0.2421	3.8167	33.5	(001)	WO <sub>3</sub>
	24.4513	0.3260	3.6376	24.9	(200)	WO <sub>3</sub>
	31.7989	0.2514	2.8118	32.9	(100)	ZnO
	33.5030	0.2794	2.6726	29.7	(02-1)	WO <sub>3</sub>
	34.0059	0.3166	2.6342	26.2	(2-20)	WO <sub>3</sub>
	36.3154	0.2794	2.4718	29.9	(101)	ZnO
15%	23.2873	0.3539	3.8167	22.9	(001)	WO <sub>3</sub>
	23.8181	0.2421	3.7328	33.5	(020)	WO <sub>3</sub>
	24.3582	0.2235	3.6513	36.4	(200)	WO <sub>3</sub>
	31.7989	0.3911	2.8118	21.1	(100)	ZnO
	33.4658	0.2794	2.6755	29.7	(02-1)	WO <sub>3</sub>
	34.0245	0.3353	2.6328	24.8	(2-20)	WO <sub>3</sub>
	36.3061	0.3352	2.4724	24.9	(101)	ZnO

The XRD peaks (100) and (101) for the ZnO structure were selected to determine the lattice parameters (a and c), according to the following equation 4.3 for hexagonal structure, for the samples prepared at the different WO<sub>3</sub> contents (Dintle *et al.* 2018).

$$\frac{1}{d_{hkl}^2} = \frac{4}{3} \frac{h^2 + hk + k^2}{a^2} + \frac{l^2}{c^2} \quad (4.3)$$

The effect of the WO<sub>3</sub> doping ratio on the lattice strain was determined using equation 4.4 (Ghosh and Pandey 2019). Table 4.3 lists the lattice constants and the existing strain.

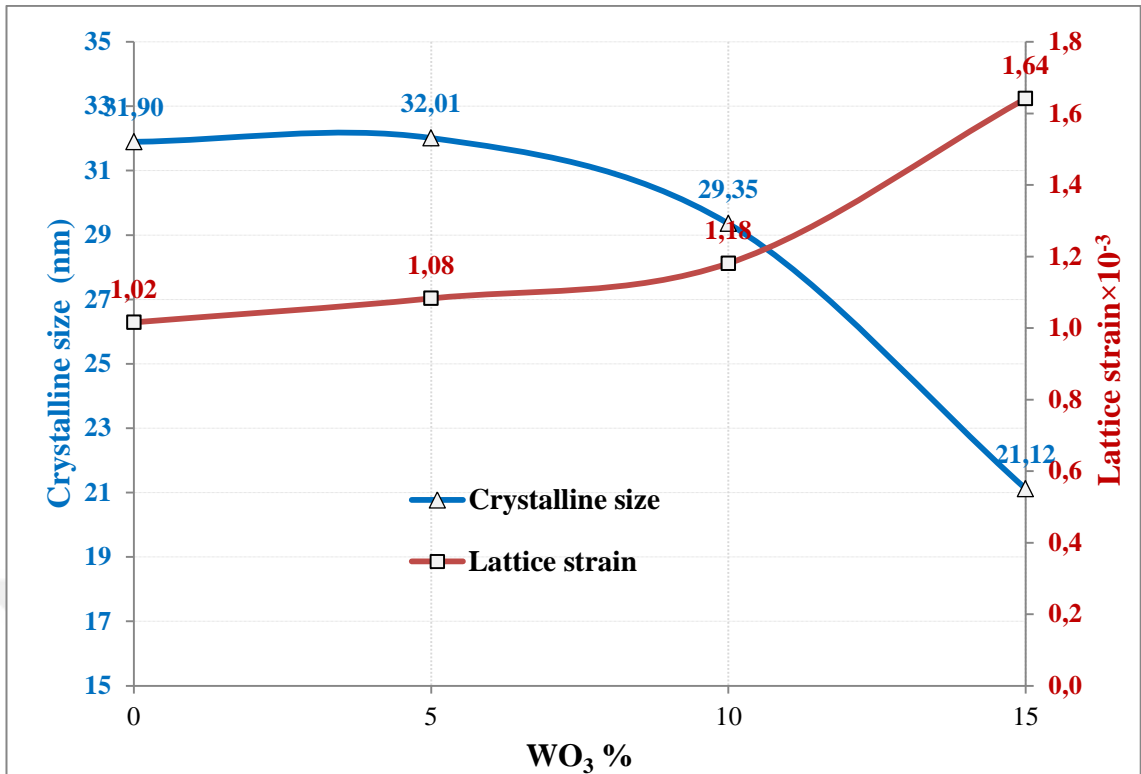
$$\varepsilon = \frac{\beta \cos\theta}{4} \quad (4.4)$$

**Table 4.3** The effect of WO<sub>3</sub> content on the lattice parameters and lattice strain for the IZO thin films

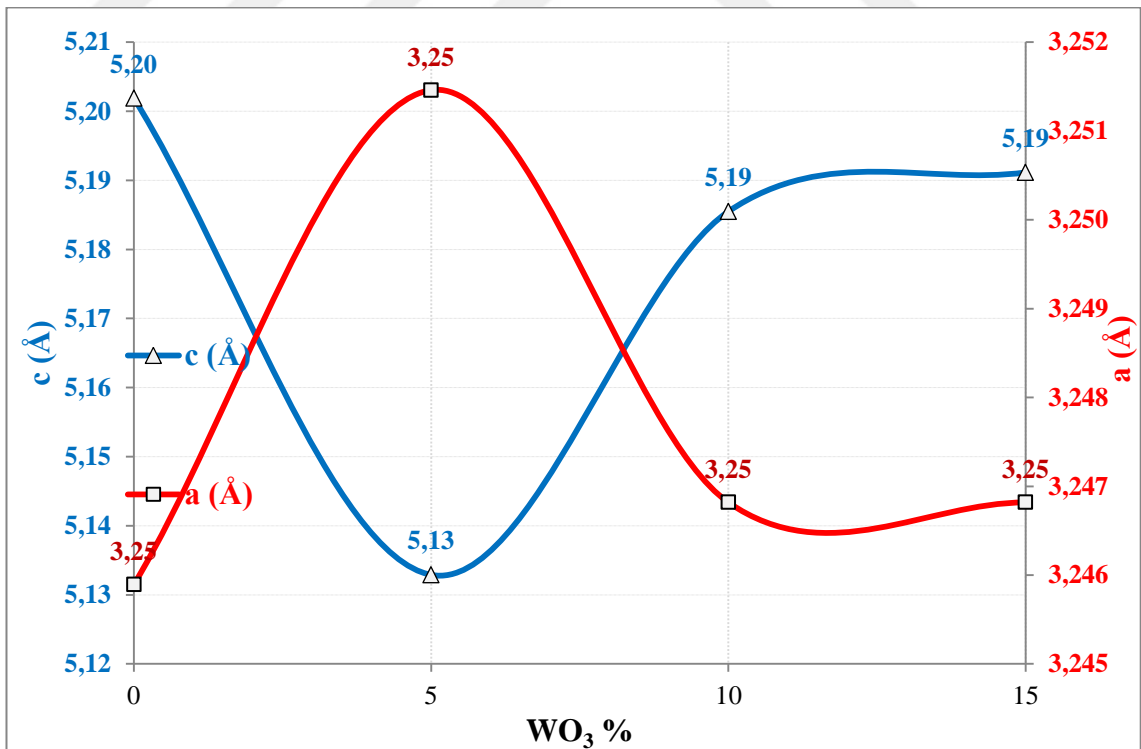
WO <sub>3</sub> %	a (Å)	c (Å)	$\epsilon \times 10^{-3}$
0	3.2459	5.2019	1.0159
5	3.2515	5.1329	1.2507
10	3.2468	5.1855	1.0550
15	3.2468	5.1911	1.6412

Figure 4.3 shows the variation of crystalline size and lattice strain along the (100) direction with the WO<sub>3</sub> content. It seems that the crystalline size reduced with growing the WO<sub>3</sub> to 15 %, while the opposite behaviour appeared for the lattice strain, as it increased with the WO<sub>3</sub> content. The primary strain induced in the lattice is due to defects due to strange atoms or due nano-size effect (Yogamalar *et al.* 2009).

Figure 4.4 illustrates the difference of lattice constants for the hexagonal ZnO structure as a function of WO<sub>3</sub> content in the IZO structure. All values of lattice constants near the expected values in the standard card. The (c) constant reduced at 5% WO<sub>3</sub> increased with more ratio. In contrast, the (a) values have opposite behaviour the fluctuation of the lattice constants due to introducing some of W atoms within the ZnO lattice.



**Figure 4.3** Crystalline size and lattice strain variation with the WO<sub>3</sub> content.



**Figure 4.4** Variation of lattice constants for ZnO with the WO<sub>3</sub> content

### 4.3 Atomic Force Microscopy

The two and three-dimensional AFM images for the ZnO, IZO, and that doped with different contents of WO<sub>3</sub> thin films deposited on glass substrate were shown in Figure 4.5. The particle size decreased from 84.1 nm for the ZnO to 25.1 nm for the IZO sample and further decreased when composed with the WO<sub>3</sub> and reduced to 25.1 nm with increasing its contents to 15%. Also, the sample surface became more smothered with the WO<sub>3</sub> content, where the root means square roughness decreased from 5.26 nm for the ZnO sample to 3.37 nm for the IZO and till reached 1.81 nm for the sample with the highest WO<sub>3</sub> ratio as listed in Table 4.4. This decrement may be due to grain size reduction (Chauhan *et al.* 2018). The thin film deposited at the high ratio of WO<sub>3</sub> appeared as a homogeneous deposition with regular particle size.

**Table 4.4** AFM results (Average Diameter and RMS roughness) for ZnO, IZO, and that doped with different contents of WO<sub>3</sub> thin films.

Samples	Average Diameter (nm)	RMS roughness (nm)
ZnO	84.1	5.26
IZO	73.3	3.37
IZO+5% WO <sub>3</sub>	41.5	2.75
IZO+10% WO <sub>3</sub>	32.0	2.50
IZO+15% WO <sub>3</sub>	25.1	1.81

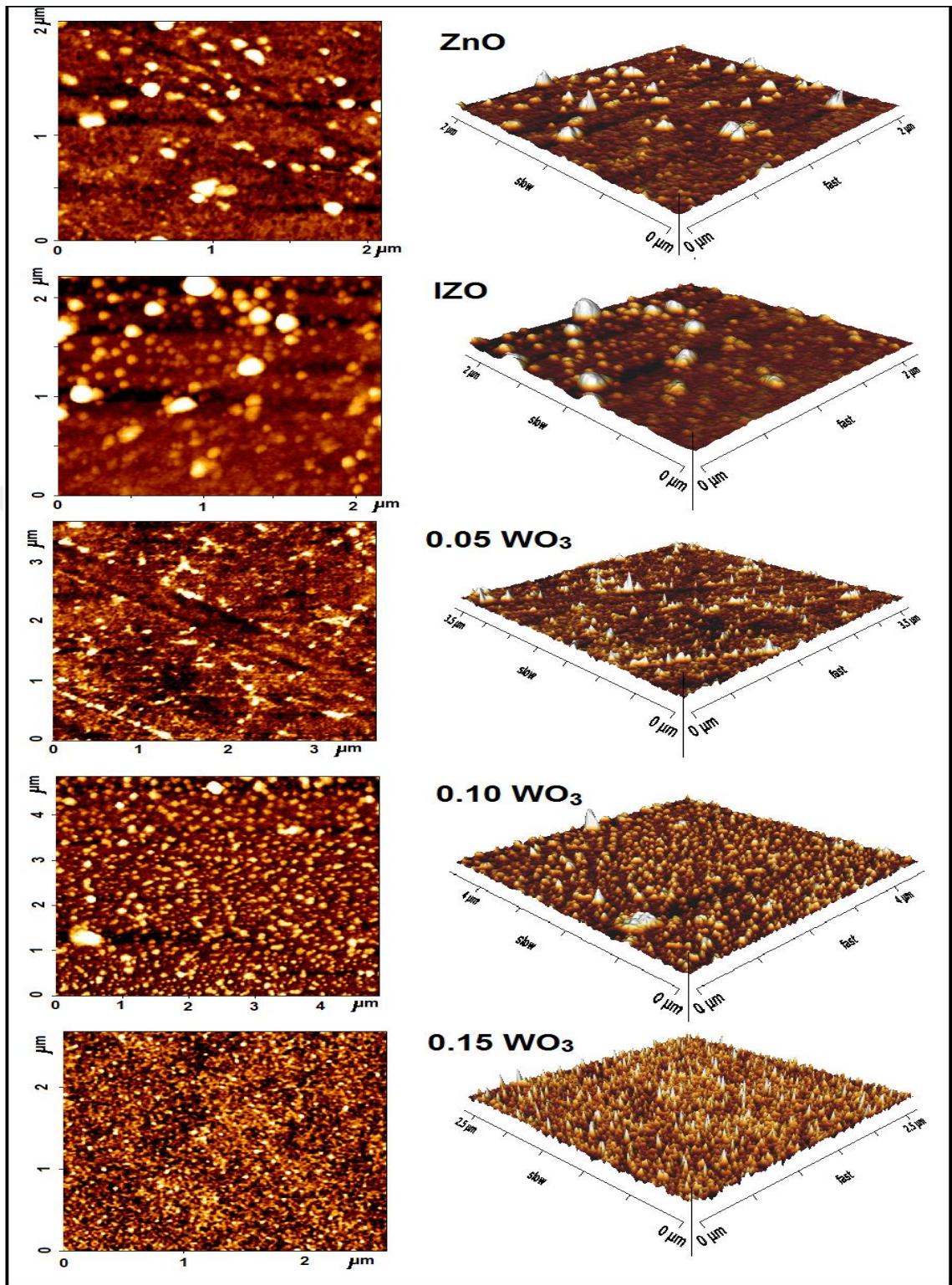


**Figure 4.5** AFM two and three-dimensional images for ZnO, IZO, and that doped with different contents of WO<sub>3</sub> thin films deposited on the glass substrate

#### 4.4 EDX Analysis

The quantitative analysis of elements was analyzed by energy-dispersive X-ray Spectroscopy (EDX). The principle of EDX depends on the fact that each element has characteristics of electronic transitions, giving an exclusive set of the electromagnetic spectrum after excitation.

Figure 4.6 demonstrates the EDX spectra for the prepared ZnO, IZO, and IZO- WO<sub>3</sub> thin film at different composition ratios on glass slides. The ZnO sample appeared as a pure sample with only lines of Zn (at 1 and 8.6 keV) and O (at 0.5 keV), and an additional peak at about 1.75 keV corresponding to Si comes from the glass substrate. Two additional peaks appeared for the indium atoms in the IZO sample (Soltabayev *et al.* 2019).

The IZO- WO<sub>3</sub> thin films samples appeared with peaks corresponding to the tungsten electronic transitions of intensities increased with increasing the WO<sub>3</sub> content. The intensities of emission lines differ depending on their presence in the samples and other parameters depending on the electronic transition probability for a specific transition (Xu and Wang 2011).

Table 4.5 illustrates the atomic and weight percentages for each element. It appears that increasing the WO<sub>3</sub> ratio cause to decrease in the oxygen content. This content is less than the stoichiometric ratio. The process might increase the oxygen vacancies, which causes an increase in the concentrations of charge carriers.

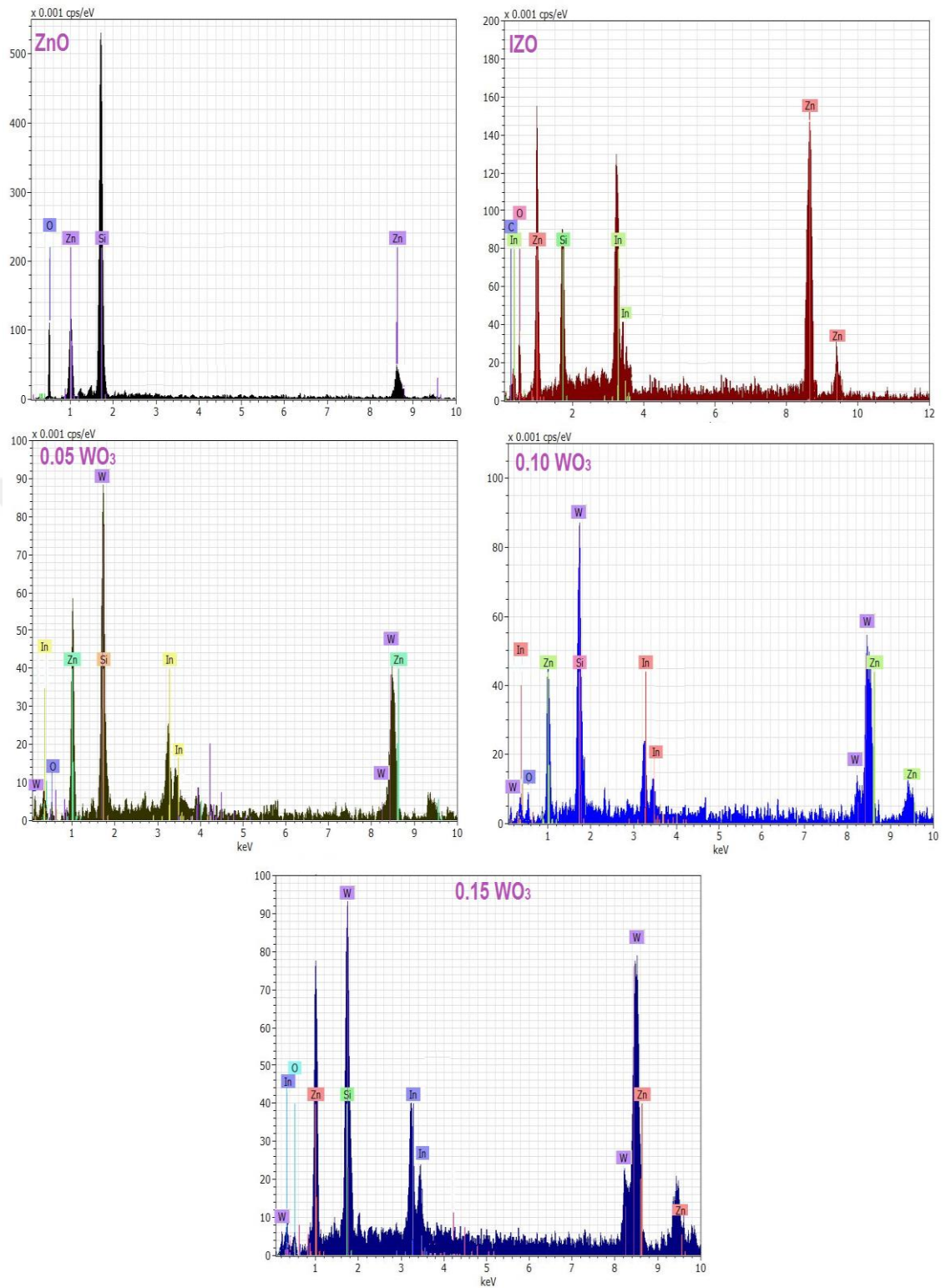


**Figure 4.6** EDX analysis for ZnO, IZO, and that doped with different contents of WO<sub>3</sub> thin films

Figure 4.7 shows that the oxygen percentage significantly reduced with increasing the  $\text{WO}_3$  content in the IZO- $\text{WO}_3$  thin film samples.

**Table 4.5** Wt% and atom % for ZnO, IZO, and that doped with different contents of  $\text{WO}_3$  thin films

Sample	Element	series	wt. %	at. %
ZnO	Zinc	K-series	60.06	26.90
	Oxygen	K-series	39.94	73.10
IZO	Indium	L-series	52.51	34.48
	Zinc	K-series	41.38	47.72
	Oxygen	K-series	6.11	17.80
0.05 $\text{WO}_3$	Tungsten	L-series	58.53	36.65
	Indium	L-series	21.24	21.30
	Zinc	K-series	17.75	31.25
	Oxygen	K-series	2.47	10.81
0.10 $\text{WO}_3$	Tungsten	L-series	67.52	45.26
	Zinc	K-series	17.08	32.19
	Indium	L-series	13.33	14.31
	Oxygen	K-series	2.07	8.25
0.15 $\text{WO}_3$	Tungsten	L-series	66.58	44.87
	Zinc	K-series	17.34	32.86
	Indium	L-series	14.08	15.20
	Oxygen	K-series	2.00	7.07

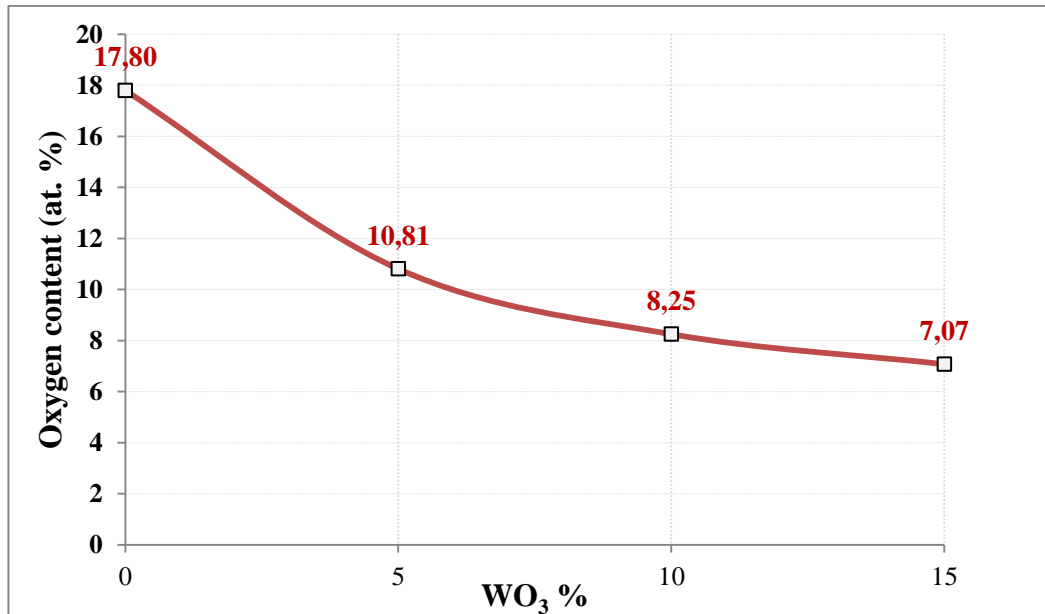


**Figure 4.7** Variation of O atomic percentage with the  $\text{WO}_3$  content

#### 4.5 Fourier Transform Infra-Red Spectroscopy

Figure 4.8 displays the FTIR transmission patterns for the ZnO, IZO, and IZO: WO<sub>3</sub> at different WO<sub>3</sub> contents prepared by PLD on glass slides between 400 to 4.000 cm<sup>-1</sup>. All spectra display significant frequency bands at 645 nm and 528 nm for Zn-O vibration, while the bands at 914.67 nm and 808 nm for Zn-OH vibrations (Qin *et al.* 2014).

The absorption bands around 3437, 1565, and 1416 cm<sup>-1</sup> correspond to the stretching vibration modes of the O-H band (Kumar *et al.* 2014).

The absorption band at around 1017 cm<sup>-1</sup> corresponds to the O-W-O vibrations, and around 740 cm<sup>-1</sup> for the W-O-W vibration appeared in samples with a higher ratio of WO<sub>3</sub> and increased intensity with its content. These bands are recognized as the characteristic bands of the WO<sub>3</sub> vibrations (Kowalkińska *et al.* 2022, Van Pham *et al.* 2022).

2973 cm<sup>-1</sup> and 2874 cm<sup>-1</sup> corresponding to the asymmetric and symmetric vibrations for the CH<sub>2</sub> group, while that at 1642.67 cm<sup>-1</sup> corresponding to the C=O band (Ceron *et al.* 2021), these organic bands absorbed from the surrounding ambient. All the mentioned bands are shown in Table 4.6.

**Table 4.6** FTIR bands for ZnO, IZO, and that doped with different contents of WO<sub>3</sub> thin films

Band Type	ZnO	IZO	0.05 WO <sub>3</sub>	0.10 WO <sub>3</sub>	0.15 WO <sub>3</sub>
O-H	3437.33	3440.00	3437.33	3442.67	3432.00
C-H asymmetric stretch	2981.33	2973.33	2973.33	3002.67	2976.00
C-H symmetric stretch	-	2874.67	2885.33	2890.67	2877.33
C=O	1642.67	1642.67	1640.00	1650.67	1637.33
O-H	1565.33	1565.33	1560.00	1578.67	1562.67
	1416.00	1413.33	1416.00	1416.00	1413.33
O-W-O	-	-	-	1017.60	1020.94
Zn-OH	914.67	914.67	914.67	922.67	922.67
	808.00	808.00	810.67	808.00	808.00
W-O-W	-	-	740.52	747.19	740.52
Zn-O	645.33	642.67	640.00	648.00	645.33
	528.00	528.00	533.33	522.67	522.67

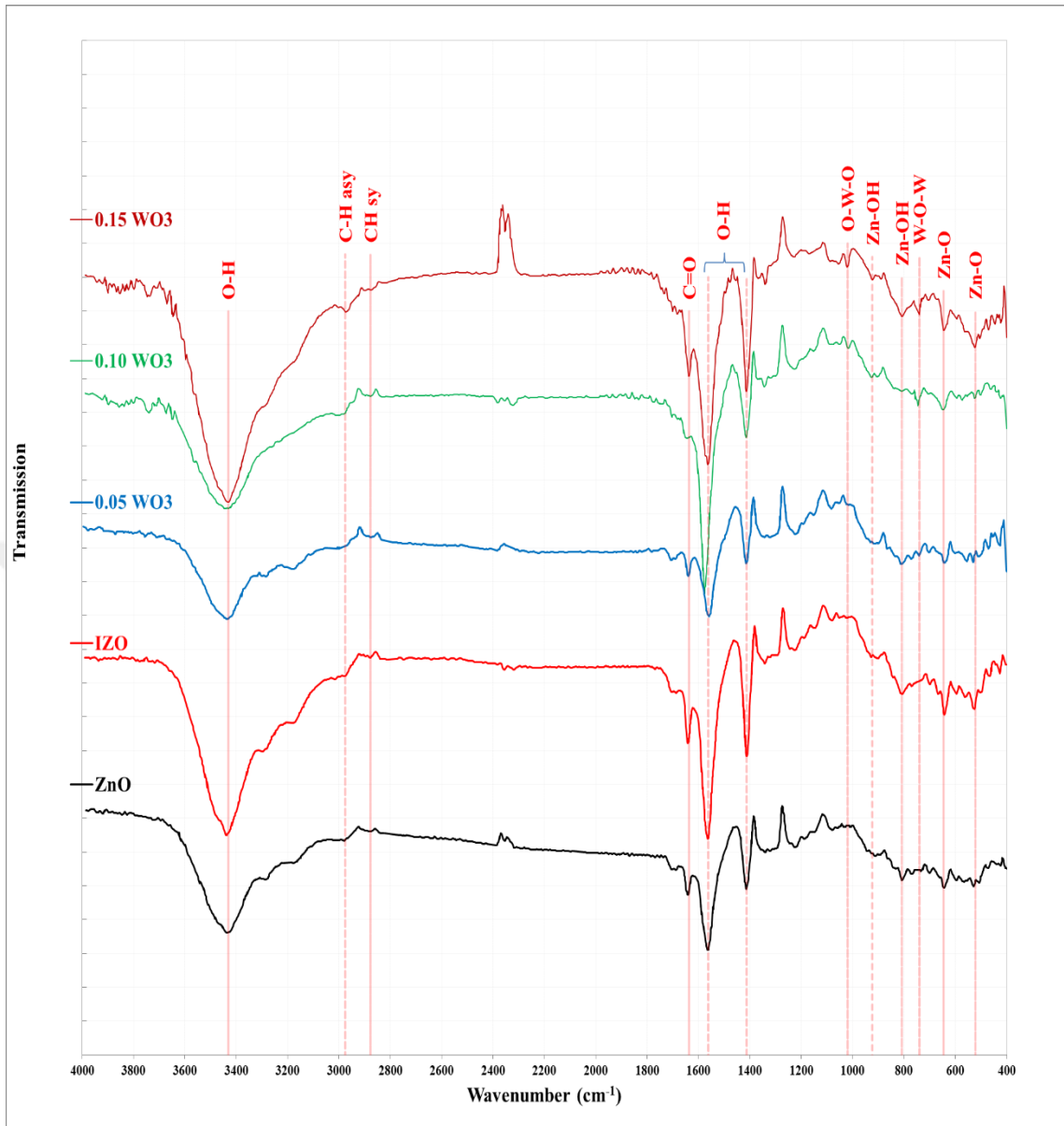


**Figure 4.8** FTIR patterns for ZnO, IZO, and that doped with different contents of WO<sub>3</sub> thin films

#### 4.6 Optical Properties

Figure 4.9 displays the optical absorption spectra in the 300-900 nm wavelength range of the ZnO, IZO, and IZO: WO<sub>3</sub> composite thin films produced by pulsed laser deposition on glass substrate at varying percentages of WO<sub>3</sub>.

All spectra appeared of gradient absorption edge due to its low crystallinity, as shown by the XRD. The preparation of IZO, as well as increasing the  $\text{WO}_3$  reason for the increase in the sample absorption. This increase is due to increasing the defects and the number of grain boundaries due to reducing the crystalline size. These boundaries act as a point of optical scattering (Mei-Zhen *et al.* 2019).

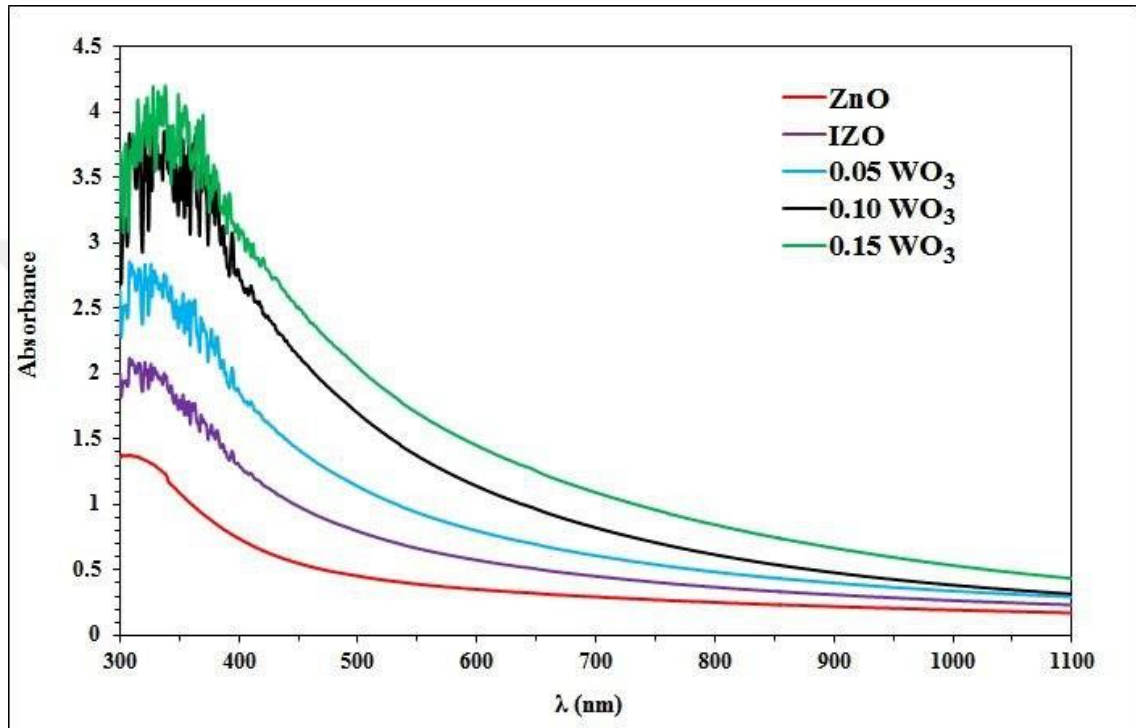


**Figure 4.9** UV-vis. optical absorption for ZnO, IZO, and that doped with different contents of  $\text{WO}_3$  thin films

The absorption coefficient ( $\alpha$ ) for the ZnO, IZO, and IZO:  $\text{WO}_3$  films at different ratios were determined using Equation (2.5), as shown in Figure 4.10. All films have a high absorption coefficient (greater than  $10^4 \text{ cm}^{-1}$ ), especially at short wavelengths indicating direct transition (Solís-Cortés *et al.* 2019).

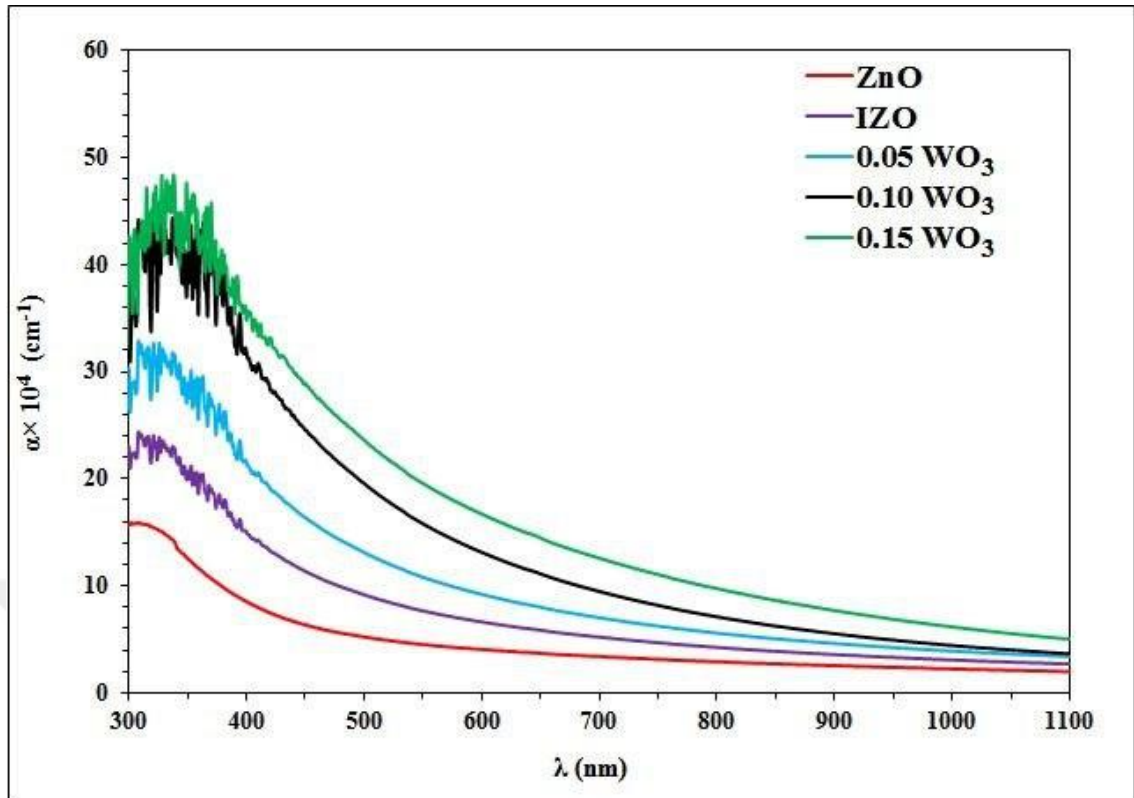


**Figure 4.10** Absorption coefficient as a function of wavelength for ZnO, IZO, and that doped with different contents of WO<sub>3</sub> thin films

The optical band-gap  $E_g^{opt}$  of the ZnO, IZO, and IZO:WO<sub>3</sub> was determined using the Tauc relation (Tiwari *et al.* 2018) equation 2.6. The relation of  $(\alpha h\nu)^2$  against the photon energy ( $h\nu$ ) is shown in Figure 4.11. The band gap values were extrapolated from the cross of the tangent line of the linear part of the curve with the x-axis, as listed in Table 4.7. The optical band gap for the ZnO thin films was observed at 3.2 eV. The band gap decreases for the IZO sample to 2.8 eV compared with the ZnO sample. This value agrees with a previous study (Dintle *et al.* 2018). Increasing the WO<sub>3</sub> content causes a reduction in the band gap gradually till it reaches 2.1 eV. The compared wavelength of this band gap is about 590 nm which is in the middle of the solar spectrum. This decrement may be attributed to the combination of the host material with the added WO<sub>3</sub>. This behaviour agrees with (Van Pham *et al.* 2022).

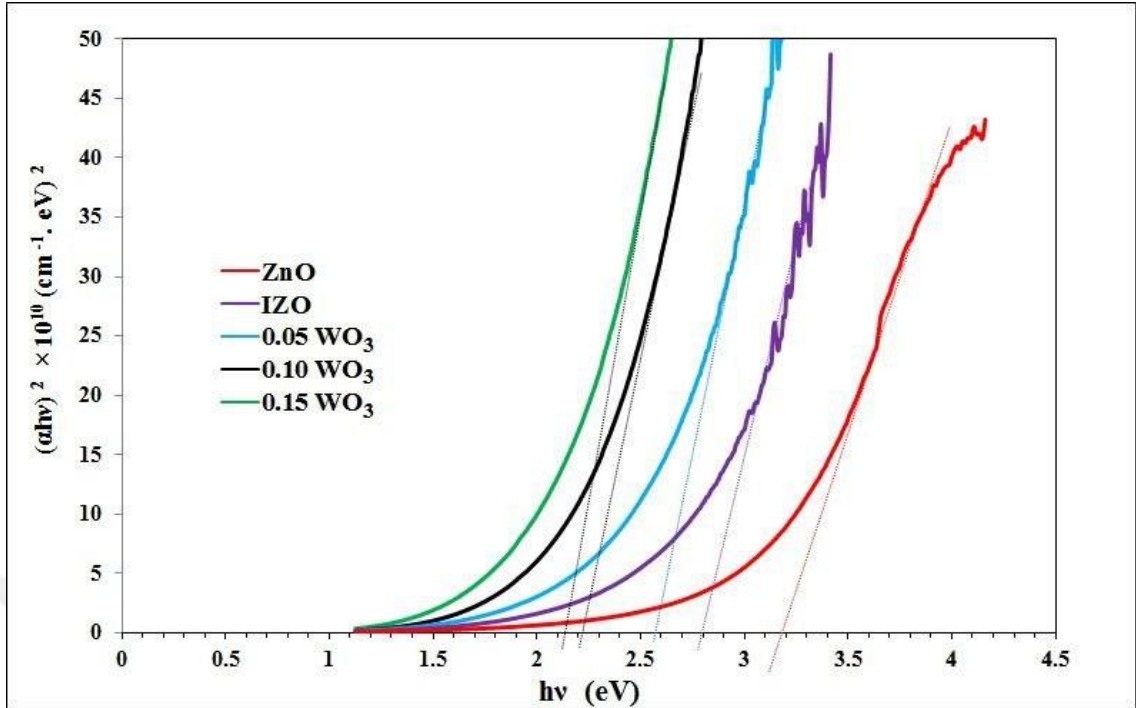


**Figure 4.11**  $(\alpha hv)^2$  versus  $(hv)$  for ZnO, IZO, and that doped with different contents of  $WO_3$  thin films

**Table 4.7** The optical band gap for ZnO, IZO- $WO_3$  thin films at different ratios

Samples	$E_g$ (eV)
ZnO	3.2
IZO	2.8
IZO+5% $WO_3$	2.6
IZO+10% $WO_3$	2.2
IZO+15% $WO_3$	2.1

#### 4.7 Hall Effect Measurements

Hall Effect measurement is used to study the electrical properties of semiconductor thin films, which include specifying the type of majority carriers, charge carriers concentration, their mobility, and the conductivity of the sample. Table 4.8 shows the Hall effect parameters for the ZnO, IZO, and IZO:  $WO_3$  composite thin film samples. All films were n-type as the negative Hall resistance (RH). The variation of NH and  $\mu H$  with the  $WO_3$  starting ratio were displayed in Figure 4.12. The charge carrier

concentration decreases from  $0.72 \times 10^{17}$  to  $8.58 \times 10^{17} \text{ cm}^{-3}$  with increasing the  $\text{WO}_3$  content to 15%, as a result of increasing the oxygen vacancies, which is the main responsible for the concentration of the charge carriers. While the mobility reduced from 249.11 to  $165.35 \text{ cm}^2/\text{V.s}$  due to increasing the grain boundaries against the charge carriers with decreasing the crystalline size, as shown by the XRD and AFM measurements. This behaviour was similar to that in a previous study (Wan *et al.* 2018).

Figure 4.13 shows that t  $\text{WO}_3$ , the conductivity of the sample enhanced with increasing the  $\text{WO}_3$  ratio due to its charge carriers.

**Table 4.8** Hall effect parameters for ZnO, IZO, and that doped with different contents of  $\text{WO}_3$  thin films

Sample	$R_H (\text{cm}^3 \cdot \text{C}^{-1})$	$N_H \times 10^{17} (\text{cm}^{-3})$	$\mu_H (\text{cm}^2/\text{v} \cdot \text{sec})$	$\sigma_{RT} (\Omega^{-1} \cdot \text{cm}^{-1})$	Type
ZnO	-86.88	0.72	280.51	3.23	N
IZO	-55.58	1.12	249.11	4.48	N
0.05	-33.57	1.86	198.76	5.92	N
0.10	-11.75	5.32	170.91	14.54	N
0.15	-7.28	8.58	165.35	22.71	N

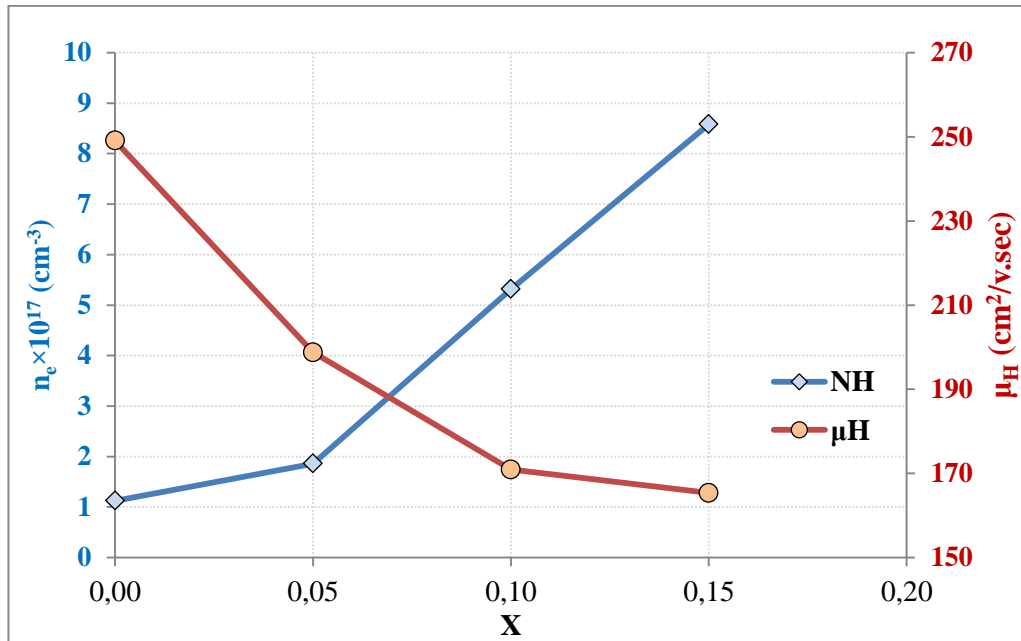


**Figure 4.12** Charge carrier concentration and their mobility variation with the  $\text{WO}_3$  contents in the IZO thin films samples

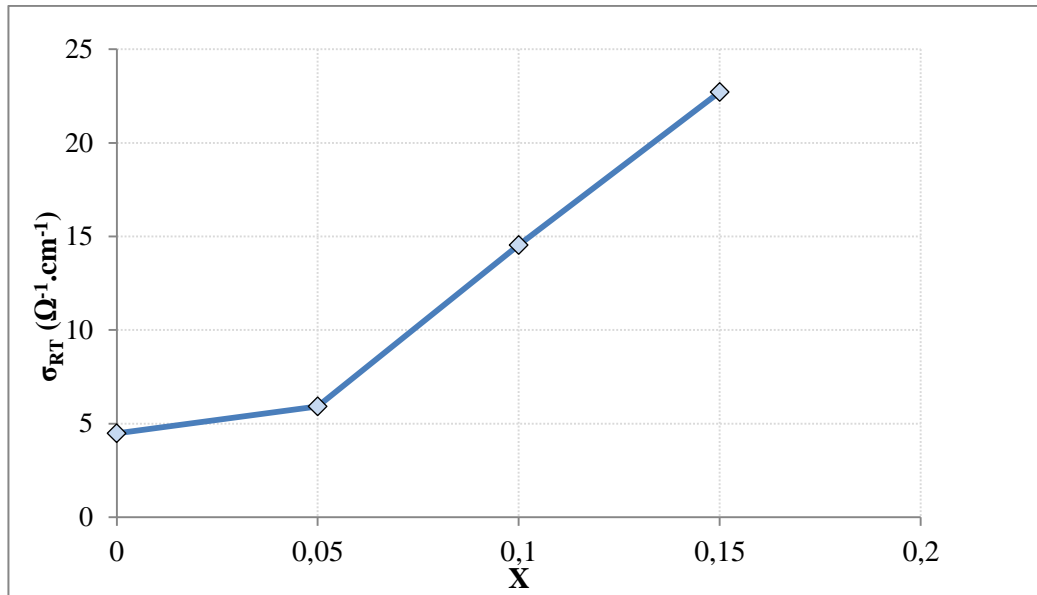


**Figure 4.13** DC conductivity variation with the  $\text{WO}_3$  contents in the IZO thin films samples

#### 4.8 I-V Characteristics

The current-voltage features of the heterojunction ZnO/ p-Si, IZO/ p-Si, and IZO:  $\text{WO}_3$ /p-Si at different  $\text{WO}_3$  ratios were examined in two bias directions (forward and reverse) at room temperature under light elimination of  $100 \text{ mW/cm}^2$  within the voltage range -0.5 to 1 V as illustrated in Figure 4.14.

The primary behaviour of these curves is their exponential behaviour. The current flows in the forward direction higher than in the reverse direction. In general, the dark forward current is produced from the flow of majority carriers due to the injection of these carriers cause to reduce the potential barrier by decreasing the width of the depletion layer (Ceron *et al.* 2021, Kim *et al.* 2021).

The photovoltaic effect is based on photon absorption, which induces electron-hole pair formation followed by charge separation with the help of a junction. The I-V curves under illumination exhibit a photovoltaic effect where the curves shift downward than the origin point due to the photocurrent.

The open circuit voltage  $V_o$  and the short circuit current  $I_{sc}$  were determined from the cross of the curve with the two axes. The maximum power was determined, represented by a rectangular area with dimensions  $I_m \times V_m$ , as shown in Figure 4.14 (Ullah *et al.* 2020).

The solar cell efficiency was determined by dividing the maximum power over the incident light power equal to the light intensity ( $100 \text{ mW/cm}^2$ ) across the working area ( $1 \text{ cm}^2$ ). The solar cell specification differs from one sample to another according to the properties of the deposited thin film.

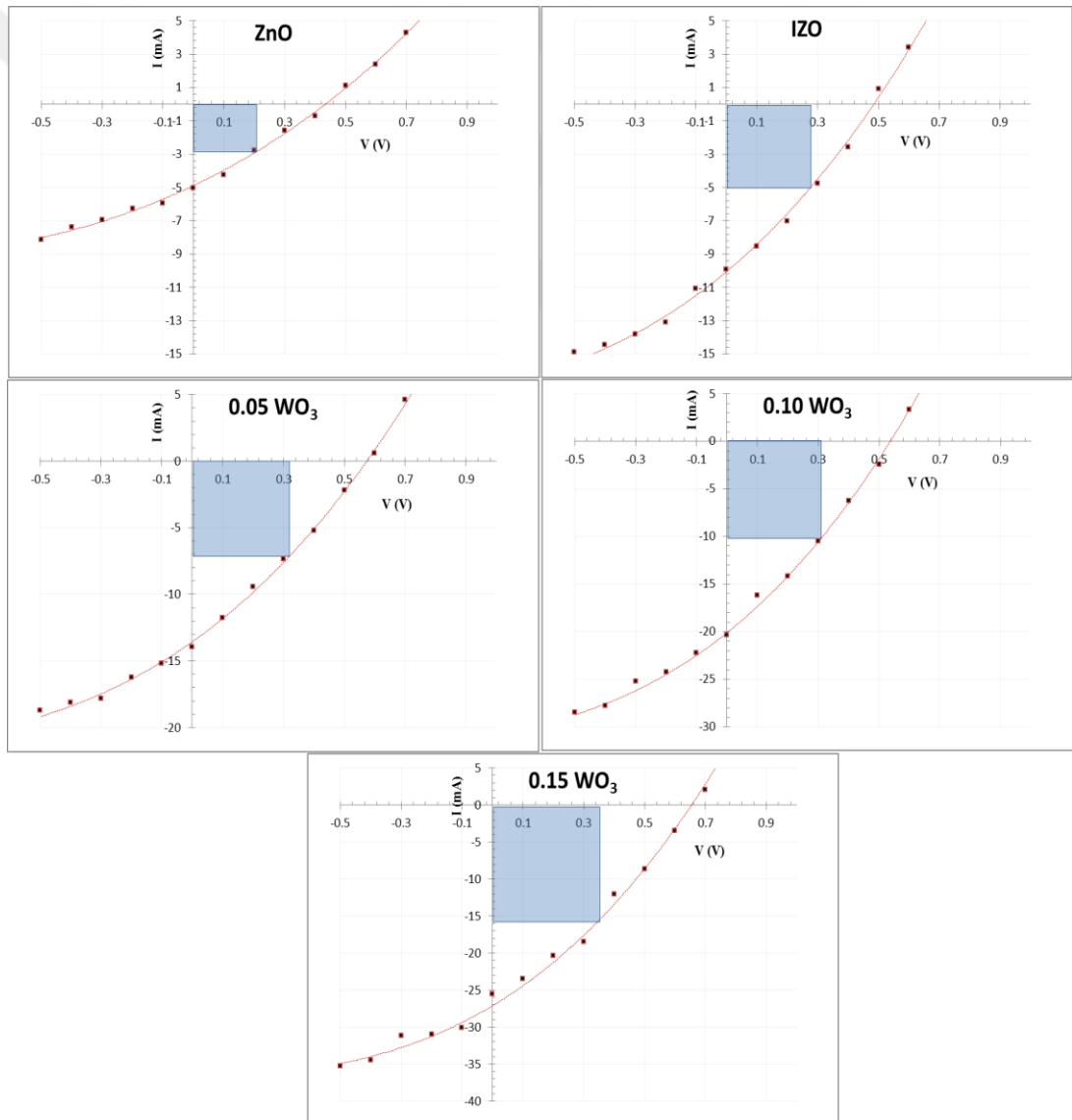


**Figure 4.14** I-V characteristics for ZnO, IZO, and IZO: WO<sub>3</sub>/P-Si heterojunctions

Table 4.9 shows photovoltaic parameters for deposited heterojunctions. This table shows that the best sample is IZO: WO<sub>3</sub> /P-Si with a 0.15 ratio of the highest efficiency value ( $\eta=5.60\%$ ). This result may be due to the higher conductivity than the other samples, reducing charge recombination losses between the generated electron-hole pairs. So, optimizing the semiconductor conductivity may enhance solar efficiency (Le Corre *et al.* 2019).

**Table 4.9** Solar cell characterization for ZnO, IZO, and IZO: WO<sub>3</sub>/P-Si heterojunctions

Sample	I <sub>sc</sub> (mA)	V <sub>oc</sub> (V)	I <sub>m</sub> (mA)	V <sub>m</sub> (V)	FF	Efficiency %
ZnO	5.2	0.5	3.0	0.21	0.27	0.63
IZO	10.5	0.5	5.1	0.28	0.30	1.43
0.05 WO <sub>3</sub>	14.5	0.6	7.0	0.32	0.28	2.24
0.10 WO <sub>3</sub>	21.0	0.6	10.5	0.31	0.28	3.26
0.15 WO <sub>3</sub>	28.0	0.7	16.0	0.35	0.31	5.60

## 5. CONCLUSIONS AND RECOMMENDATION

### 5.1 Conclusions

Thin films of ZnO, IZO, and IZO: WO<sub>3</sub> of good performance were prepared by a one-step pulsed laser deposition technique. The properties of the IZO thin film study show the practical tuning by composing with WO<sub>3</sub>, which is indicated by different characterization techniques. Different techniques showed the following result.

The x-ray diffraction (XRD) shows that composing the IZO with different ratios of WO<sub>3</sub> causes to high effect on lattice constants, crystalline size, and lattice strain. The crystalline size reduced with increasing the WO<sub>3</sub> to 15 %, while the opposite behavior appeared for the lattice strain and fluctuation of the lattice constants. These variations in structural properties highly affect other physical properties. The AFM test shows reducing the particle size and surface roughness with the WO<sub>3</sub> contents. The quantitative analysis of elements by EDX shows that increasing the WO<sub>3</sub> ratio causes to decrease in the oxygen content, indicating an increase in oxygen vacancies and enhancing carrier concentration. The FTIR studies the characteristics band for the composition. The optical absorption slightly increases, and the energy bandgap is reduced from 2.8 to 2.1 eV with the WO<sub>3</sub> content. Hall Effect measurement shows that all films were n-type, charge carrier mobility decreased, While the mobility reduced, and the conductivity enhanced with WO<sub>3</sub> content.

Although the low cost of the prepared heterojunctions, it shows distinct characteristics. The I-V characteristics of the prepared ZnO/p-Si, IZO/p-Si, and IZO: WO<sub>3</sub>/p-Si heterojunction at different WO<sub>3</sub> ratios shows photovoltaic behavior, and the best sample that is with the 15% ratio of the highest efficiency value  $\eta = 5.60\%$ . However, the low efficiency of the obtained heterojunctions has a low preparation cost. In addition, it can be used as a photodetector.

## 5.2 Recommendations for Future Works

- Enhancing the prepared solar cell with plasmonic nanoparticles such as gold nanoparticles.
- Enhancing the prepared solar cell with an anti-reflected coating.
- Experience electrodes of different types of metals and experience their ohmic contact.



## REFERENCES

- Abrutis, A., Valincius, G., Baltrunas, G., Parafionovic, L., Valiuniene, A. and Saltyte, Z. 2007. Spray-pyrolysis  $\text{Cd}_2\text{SnO}_4$  films for electrochemical applications. *Thin Solid Films*, 515(17): 6817-6823.
- Acosta, E. 2021. Thin Films/Properties and Applications. In *Thin Films*. IntechOpen.
- Akkurt, N., Pat, S., Elmas, S. and Korkmaz, Ş. 2020. Electrochromic properties of UV-colored  $\text{WO}_3$  thin film deposited by thermionic vacuum arc. *Journal of Materials Science: Materials in Electronics*, 31(2): 1293-1301.
- Babar, A. R., Shinde, S. S., Moholkar, A. V., Bhosale, C. H., Kim, J. H. and Rajpure, K. Y. 2011. Physical properties of sprayed antimony doped tin oxide thin films: The role of thickness. *Journal of Semiconductors*, 32(5): 053001.
- Barhdadi, A., Hartiti, B. and Muller, J. C. C. 2012. Active defects generated in silicon by laser doping process. *The African Review of Physics*, 6.
- Bel-Hadj-Tahar, R. and Mohamed, A. B. 2014. Sol-gel processed indium-doped zinc oxide thin films and their electrical and optical properties. *New Journal of Glass and Ceramics*, 4(04): 55.
- Bragg, W. H. and Bragg, W. L. 1918. *X Rays and Crystal Structure*. G. Bell and Sons, Ltd.
- Brodiskiy, M. H. 1979. *Amorphous Semiconductors*. Springer-Verlage.
- Cappella, B. and Dietler, G. 1999. Force-distance curves by atomic force microscopy. *Surface science reports*, 34(1-3): 1-104.
- Ceron, S., Orduña-Díaz, A. and Dominguez, M. A. 2021. Influence of inductive effect in organic residuals content in IZO thin films and the performance on the behaviour of MIS capacitors on plastic. *Engineering Proceedings*, 4(1): 9.
- Chauhan, R. N., Tiwari, N., Shieh, H. P. D. and Liu, P. T. 2018. Electrical performance and stability of tungsten indium zinc oxide thin-film transistors. *Materials Letters*, 214, 293-296.
- Chen, S., Zhang, Q., Hou, Y., Zhang, J. and Liang, X. J. 2013. Nanomaterials in medicine and pharmaceuticals: nanoscale materials developed with less toxicity and more efficacy. *European Journal of Nanomedicine*, 5(2): 61-79.

- Chen, Y. 2018. Review of ZnO transparent conducting oxides for solar applications. In IOP Conference Series: Materials Science and Engineering (Vol. 423, No. 1, p. 012170). IOP Publishing.
- Chiang, Y. H., Peng, C. C., Chen, Y. H., Tung, Y. L., Tsai, S. Y. and Chen, P. 2018. The utilization of IZO transparent conductive oxide for tandem and substrate type perovskite solar cells. *Journal of Physics D: Applied Physics*, 51(42): 424002.
- Cho, M., Eom, T. Y., Nundy, S., Park, J. S. and Lee, H. J. 2021. Conductometric nitrogen dioxide gas sensors based on sol-gel-prepared hafnium-added indium zinc oxide (Hf-IZO). *Sensors and Actuators B: Chemical*, 344, 130198.
- Chopra, K. N. and Maini, A. K. 2010. Thin films and their applications in military and civil sectors. Ministry of Defence, New Delhi.
- Chrisey, D. B. and Hubler, G. K. 1994. Pulsed laser deposition of thin films.
- Craciun, V., Martin, C., Socol, G., Tanner, D., Swart, H. C., Becherescu, N. and Craciun, D. 2014. Optical properties of amorphous indium zinc oxide thin films synthesized by pulsed laser deposition. *Applied surface science*, 306, 52-55.
- De Mello Donegá, C. 2014. Nanoparticles: Workhorses of nanoscience. Springer.
- Dhamodharan, P., Chen, J. and Manoharan, C. 2021. Fabrication of In doped ZnO thin films by spray pyrolysis as photoanode in DSSCs. *Surfaces and Interfaces*, 23, 100965.
- Dintle, L. K., Luhanga, P. V., Moditswe, C. and Muiva, C. M. 2018. Compositional dependence of optical and electrical properties of indium doped zinc oxide (IZO) thin films deposited by chemical spray pyrolysis. *Physica E: Low-Dimensional Systems and Nanostructures*, 99, 91-97.
- Diwald, O. and Hartmann, M. 2021. Adsorption and Chemical Reactivity. *Metal Oxide Nanoparticles: Formation, Functional Properties, and Interfaces*, 2, 593-636.
- Djelloul, A., Larbah, Y., Adnane, M., Labdelli, B., Ziane, M. I., Manseri, A. and Messaoud, A. 2018. Properties of undoped and (Al, In) doped ZnO thin films prepared by ultrasonic spray pyrolysis for solar cell applications.
- Dresselhaus, M. S. 2001. Transport Properties of Solids. Lecture Notes. In:-Solid State Physics-Part 1.
- Eason, R. 2007. Pulsed laser deposition of thin films: applications-led growth of functional materials. John Wiley and Sons.

- Ge, C., Wang, M., Hussain, S., Xu, Z., Liu, G. and Qiao, G. 2018. Electron transport and electrochromic properties of sol-gel WO<sub>3</sub> thin films: Effect of crystallinity. *Thin Solid Films*, 653, 119-125.
- Ghosh, K. and Pandey, R. K. 2019. Fractal and multifractal analysis of In-doped ZnO thin films deposited on glass, ITO, and silicon substrates. *Applied Physics A*, 125(2): 1-11.
- Greiner, R. A. 1961. *Semiconductor Device*. Electronic Energy Series, McGraw-Hill Book Co. Inc.
- Greiner, R. A. and Eggers, J. 1989. The spectral amplitude distribution of selected compact discs. *Journal of the Audio Engineering Society*, 37(4): 246-275.
- Gurumurthy, S., Bhat, H. L. and Kumar, V. 1999. Excellent rectifying characteristics in Au/n-CdTe diodes upon exposure to rf nitrogen plasma. *Semiconductor science and technology*, 14(10): 909.
- Hall, E. H. 1879. On a new action of the magnet on electric currents. *American Journal of Mathematics*, 2(3): 287-292
- Horikoshi, S. and Serpone, N. 2013. *Microwaves in nanoparticle synthesis: fundamentals and applications*. John Wiley and Sons.
- Jain, V. K. and Vijay, Y. K. 2016. Formation of In<sub>2</sub>O<sub>3</sub>-ZnO Thin Films and Post Annealing Influence on Optical Properties. In *Proceedings of the International MultiConference of Engineers and Computer Scientists*. 2: 13-15.
- Jiang, J., Pi, J. and Cai, J. 2018. The advancing of zinc oxide nanoparticles for biomedical applications. *Bioinorganic chemistry and applications*, 2018.
- Jiang, W., Ji, W. and Au, C. T. 2018. Surface/interfacial catalysis of (metal)/oxide system: structure and performance control. *ChemCatChem*, 10(10): 2125-2163.
- Kalantar-Zadeh, K. and Fry, B. 2008. *Organic Nanotechnology Enabled Sensors*, pp. 371-481, Springer US.
- Kazmerski, L. 2012. *Polycrystalline and amorphous thin films and devices*. Elsevier.
- Khan, I., Saeed, K. and Khan, I. 2019. Nanoparticles: Properties, applications and toxicities. *Arabian journal of chemistry*, 12(7): 908-931.
- Khashan, K. S. and Mahdi, M. 2017. Preparation of indium-doped zinc oxide nanoparticles by pulsed laser ablation in liquid technique and their characterization. *Applied Nanoscience*, 7(8): 589-596.

- Khusayfan, N. M., Al-Ghamdi, A. A. and Yakuphanoglu, F. 2016. Solar light photodetectors based on nanocrystalline copper indium oxide/p-Si heterojunctions. *Journal of Alloys and Compounds*, 663: 796-807.
- Kim, M. J., Park, H. W., Jeong, K. and Chung, K. B. 2021. In-Situ Investigation of the Gate Bias Instability of Tungsten-Doped Indium Zinc Oxide Thin Film Transistor by Simultaneous Ultraviolet and Thermal Treatment. *IEEE Transactions on Electron Devices*, 68(8): 3851-3856.
- Kiriakidis, G., Bender, M., Katsarakis, N., Gagaoudakis, E., Hourdakis, E., Douloufakis, E. and Cimalla, V. 2001. Ozone sensing properties of polycrystalline indium oxide films at room temperature. *physica status solidi (a)*: 185(1): 27-32.
- Kittel, C. 1955. *Solid state physics*. Shell Development Company. 3: 437-564.
- Kohl, P. A. 1998. Photoelectrochemical etching of semiconductors. *IBM journal of research and development*, 42(5): 629-638.
- Kołodziejczak-Radzimska, A. and Jesionowski, T. 2014. Zinc oxide—from synthesis to application: a review. *Materials*, 7(4): 2833-2881.
- Koole, R., Groeneveld, E., Vanmaekelbergh, D., Meijerink, A. and Mello Donegá, C. D. 2014. Size effects on semiconductor nanoparticles. In *Nanoparticles* (pp. 13-51). Springer, Berlin, Heidelberg.
- Kowalkińska, M., Fiszka Borzyszkowska, A., Grzegórska, A., Karczewski, J., Głuchowski, P., Łapiński, M. and Zielińska-Jurek, A. 2022. Pilot-Scale Studies of WO<sub>3</sub>/S-Doped g-C<sub>3</sub>N<sub>4</sub> Heterojunction toward Photocatalytic NO<sub>x</sub> Removal. *Materials*, 15(2): 633.
- Kumar, H., Singh, J. P., Srivastava, R. C., Negi, P., Agrawal, H. M. and Asokan, K. 2014. FTIR and electrical study of dysprosium doped cobalt ferrite nanoparticles. *Journal of Nanoscience*, 2014.
- Kusumawati, Y. 2015. Oxide and composite electron transport layers for efficient dye-sensitized solar cells (Doctoral dissertation, Université Pierre et Marie Curie-Paris VI; Institut teknologi Bandung).
- Lang, K. M., Hite, D. A., Simmonds, R. W., McDermott, R., Pappas, D. P. and Martinis, J. M. 2004. Conducting atomic force microscopy for nanoscale tunnel barrier characterization. *Review of scientific instruments*, 75(8): 2726-2731.

- Le Corre, V. M., Stolterfoht, M., Perdigon Toro, L., Feuerstein, M., Wolff, C., Gil-Escrig, L. and Koster, L. J. A. 2019. Charge transport layers limiting the efficiency of perovskite solar cells: how to optimize conductivity, doping, and thickness. *ACS Applied Energy Materials*, 2(9): 6280-6287.
- Le, M. N., Kim, H., Kang, Y. K., Song, Y., Guo, X., Ha, Y. G. and Kim, M. G. 2019. Bulk charge-transfer doping of amorphous metal oxide: fullerene blends for solution-processed amorphous indium zinc oxide thin-film transistors. *Journal of Materials Chemistry C*, 7(34): 10635-10641.
- Lehmann, V. and Föll, H. 1990. Formation mechanism and properties of electrochemically etched trenches in n-type silicon. *Journal of the Electrochemical Society*, 137(2): 653.
- Lin, D., Li, K., Shao, J. and Zhang, Q. 2019. High-performance thin-film transistors with nickel-doped indium zinc oxide channel layers. *physica status solidi (a)*: 216(18): 1900274.
- Lin, Y. H. 2010. Structure and properties of transparent conductive ZnO films grown by pulsed laser deposition (PLD) (Doctoral dissertation, University of Birmingham).
- Lindberg, O. 1952. Hall effect. *Proceedings of the IRE*, 40(11): 1414-1419.
- Liu, R., Chen, Y., Ding, S., Li, Y. and Tian, Y. 2019. Preparation of highly transparent conductive aluminum-doped zinc oxide thin films using a low-temperature aqueous solution process for thin-film solar cells applications. *Solar Energy Materials and Solar Cells*, 203, 110161.
- Lu, J. G., Chang, P. and Fan, Z. 2006. Quasi-one-dimensional metal oxide materials—Synthesis, properties and applications. *Materials Science and Engineering: R: Reports*, 52(1-3): 49-91.
- Lu, K., Yao, R., Xu, W., Ning, H., Zhang, X., Zhang, G. and Peng, J. 2021. Alloy-Electrode-Assisted High-Performance Enhancement-Type Neodymium-Doped Indium-Zinc-Oxide Thin-Film Transistors on Polyimide Flexible Substrate. *Research*, 2021.
- Marezio, M. 1966. Refinement of the crystal structure of  $\text{In}_2\text{O}_3$  at two wavelengths. *Acta Crystallographica*, 20(6): 723-728.

- Mason, T. O., Harvey, S. P. and Poepelmeier, K. R. 2011. Ternary and Multinary Materials: Crystal/Defect Structure–Property Relationships. In Handbook of Transparent Conductors (pp. 265-293). Springer, Boston, MA.
- Mei-Zhen, G., Feng, Z., Jing, L. and Hui-Na, S. 2009. Effect of annealing conditions on properties of sol-gel derived Al-doped ZnO thin films. Chinese Physics Letters, 26(8): 088105.
- Minami, T. 2005. Transparent conducting oxide semiconductors for transparent electrodes. Semiconductor science and technology, 20(4): S35.
- Mott, N. F. and Davis, E. A. 2012. Electronic processes in non-crystalline materials. Oxford university press.
- Murugesan, M., Arjunraj, D., Mayandi, J., Venkatachalapathy, V. and Pearce, J. M. 2018. Properties of Al-doped zinc oxide and In-doped zinc oxide bilayer transparent conducting oxides for solar cell applications. Materials Letters, 222, 50-53.
- Napi, M. L. M., Noorden, A. F. A., Tan, M. L. P., Jamaluddin, H., Abd Hamid, F., Ahmad, M. K. and Sultan, S. M. 2020. Three Dimensional Zinc Oxide Nanostructures as an Active Site Platform for Biosensor: Recent Trend in Healthcare Diagnosis. Journal of The Electrochemical Society, 167(13): 137501.
- Neamen, D. A. 2003. Semiconductor physics and devices: basic principles. McGraw-hill.
- Ngom, B. D., Mpahane, T., Manyala, N., Nemraoui, O., Buttner, U., Kana, J. B. and Beye, A. C. 2009. Structural and optical properties of nano-structured tungsten-doped ZnO thin films grown by pulsed laser deposition. Applied Surface Science, 255(7): 4153-4158.
- Paramasivam, G., Palem, V. V., Sundaram, T., Sundaram, V., Kishore, S. C. and Bellucci, S. 2021. Nanomaterials: Synthesis and applications in theranostics. Nanomaterials, 11(12): 3228.
- Qin, N., Xiang, Q., Zhao, H., Zhang, J., and Xu, J. 2014. Evolution of ZnO microstructures from hexagonal disk to prismoid, prism and pyramid and their crystal facet-dependent gas sensing properties. CrystEngComm, 16(30): 7062-7073.
- Rai, H. C. and Raj, A. 2004. Question bank in electrical and electronics engineering. Galgotia publication Pvt. Ltd.

- Rajput, J. K. and Purohit, L. P. 2016. Comparative study of synthesis of CdO-ZnO nanocomposite thin films by different methods: a review. *Nanosci. Technol.*, 3(1): 1-5.
- Rajput, N. 2015. Methods of preparation of nanoparticles-a review. *International Journal of Advances in Engineering and Technology*, 7(6): 1806.
- Saritha, D., Koirala, A. R., Venu, M., Reddy, G. D., Reddy, A. V. B., Sitaram, B., ... and Aruna, K. 2019. A simple, highly sensitive and stable electrochemical sensor for the detection of quercetin in solution, onion and honey buckwheat using zinc oxide supported on carbon nanosheet (ZnO/CNS/MCPE) modified carbon paste electrode. *Electrochimica Acta*, 313, 523-531.
- Scherrer, P. 1918. *Göttinger Nachrichten Gesell. Universität Zu Göttingen*, 2, 98.
- Shaheera, M., Girija, K. G., Kaur, M., Geetha, V., Debnath, A. K., Vatsa, R. K. and Gadkari, S. C. 2020. Characterization and device application of indium doped ZnO homojunction prepared by RF magnetron sputtering. *Optical Materials*, 101, 109723.
- Silva-Lopez, H. E., Marcelino, B. S., Guillen-Cervantes, A., Zelaya-Angel, O. and Ramirez-Bon, R. 2018. Physical properties of sputtered indium-doped ZnO films deposited on flexible transparent substrates. *Materials Research*, 21.
- Sirelkhatim, A., Mahmud, S., Seeni, A., Kaus, N. H. M., Ann, L. C., Bakhori, S. K. M. and Mohamad, D. 2015. Review on zinc oxide nanoparticles: antibacterial activity and toxicity mechanism. *Nano-micro letters*, 7(3): 219-242.
- Soga, T. 2006. *Nanostructured materials for solar energy conversion*. Elsevier.
- Solís-Cortés, D., Schrebler, R., Navarrete-Astorga, E., López-Escalante, M., Martín, F., Ramos-Barrado, J. R. and Dalchiele, E. A. 2019. Electrochemical characterization of transparent conducting IZO: Ga thin films. *Journal of Alloys and Compounds*, 808, 151776.
- Soltabayev, B., Yıldırım, M. A., Ateş, A. and Acar, S. 2019. The effect of indium doping concentration on structural, morphological and gas sensing properties of IZO thin films deposited SILAR method. *Materials Science in Semiconductor Processing*, 101, 28-36.
- Stadler, A. 2012. Transparent conducting oxides—an up-to-date overview. *Materials*, 5(4): 661-683.

- Sun, Z., Fan, Q., Zhang, M., Liu, S., Tao, H. and Texter, J. 2019. Supercritical fluid-facilitated exfoliation and processing of 2D materials. *Advanced Science*, 6(18): 1901084.
- Szkoda, M., Zarach, Z., Trzcíński, K. and Nowak, A. P. 2020. An Aqueous Exfoliation of  $\text{WO}_3$  as a Route for Counterions Fabrication—Improved Photocatalytic and Capacitive Properties of Polyaniline/ $\text{WO}_3$  Composite. *Materials*, 13(24): 5781.
- Tiwari, N., Rajput, M., John, R. A., Kulkarni, M. R., Nguyen, A. C. and Mathews, N. 2018. Indium tungsten oxide thin films for flexible high-performance transistors and neuromorphic electronics. *ACS applied materials and interfaces*, 10(36): 30506-30513.
- Tsai, D. C., Chang, Z. C., Kuo, B. H., Wang, Y. H., Chen, E. C. and Shieu, F. S. 2018. Thickness dependence of the structural, electrical, and optical properties of amorphous indium zinc oxide thin films. *Journal of Alloys and Compounds*, 743, 603-609.
- Ullah, S., Branquinho, R., Mateus, T., Martins, R., Fortunato, E., Rasheed, T. and Sher, F. 2020. Solution combustion synthesis of transparent conducting thin films for sustainable photovoltaic applications. *Sustainability*, 12(24): 10423.
- Van Pham, V., Truong, T. K., Le, H. V., Nguyen, H. T., Tong, H. D. and Cao, T. M. 2022. Enhancing Green Product Generation of Photocatalytic NO Oxidation: A Case of  $\text{WO}_3$  Nanoplate/g- $\text{C}_3\text{N}_4$  S-Scheme Heterojunction. *Langmuir*, 38(13): 4138-4146.
- Vasile, N., Iftimie, S., Acsente, T., Locovei, C., Călugăr, A. I., Radu, A. and Antohe, Ș. 2020. Physical properties of indium zinc oxide and aluminium zinc oxide thin films deposited by radio-frequency magnetron sputtering. *Materials Research Express*, 6(12): 126447.
- Walsh, A., Da Silva, J. L., Wei, S. H., Körber, C., Klein, A., Piper, L. F. J. and Egdell, R. G. 2008. Nature of the band gap of  $\text{In}_2\text{O}_3$  revealed by first-principles calculations and X-ray spectroscopy. *Physical review letters*, 100(16): 167402.
- Wan, D., Liu, X., Abliz, A., Liu, C., Yang, Y., Wu, W. and Liao, L. 2018. Design of highly stable tungsten-doped IZO thin-film transistors with enhanced performance. *IEEE Transactions on Electron Devices*, 65(3): 1018-1022.

- Wang, L., Liu, F., Cai, X., Ma, T. and Jiang, C. 2018. Indium Zinc Oxide Electron Transport Layer for High-Performance Planar Perovskite Solar Cells. *The Journal of Physical Chemistry C*, 122(50): 28491-28496.
- Wang, Y., Chen, W., Wang, B. and Zheng, Y. 2014. Ultrathin ferroelectric films: growth, characterization, physics and applications. *Materials*, 7(9): 6377-6485.
- Wankhede, P., Sharma, P. K. and Jha, A. K. 2013. Synthesis of copper nanoparticles through wire explosion route. *J. Eng. Res. Appl*, 3(6): 1664-1669.
- Winkler, N., Edinger, S., Kaur, J., Wibowo, R. A., Kautek, W. and Dimopoulos, T. 2018. Solution-processed all-oxide solar cell based on electrodeposited Cu<sub>2</sub>O and ZnMgO by spray pyrolysis. *Journal of materials science*, 53(17): 12231-12243.
- Winkler, N., Wibowo, A. R., Kubicek, B., Kautek, W., Ligorio, G., List-Kratochvil, E. J. and Dimopoulos, T. 2019. Rapid Processing of In-Doped ZnO by Spray Pyrolysis from Environment-Friendly Precursor Solutions. *Coatings*, 9(4): 245.
- Witkowski, B. S. 2018. Applications of ZnO Nanorods and Nanowires--A Review. *Acta Physica Polonica, A.*, 134(6).
- Xu, L., Liang, H. W., Yang, Y. and Yu, S. H. 2018. Stability and reactivity: positive and negative aspects for nanoparticle processing. *Chemical reviews*, 118(7): 3209-3250.
- Xu, S. and Wang, Z. L. 2011. One-dimensional ZnO nanostructures: solution growth and functional properties. *Nano Research*, 4(11): 1013-1098.
- Yogamalar, R., Srinivasan, R., Vinu, A., Ariga, K. and Bose, A. C. 2009. X-ray peak broadening analysis in ZnO nanoparticles. *Solid State Communications*, 149(43-44): 1919-1923.
- Zaien, M., Ahmed, N. M. and Hassan, Z. 2013. Fabrication and Characterization of an n-CdO/p-Si Solar Cell by Thermal Evaporation in a Vacuum,". *Int. j. Electrochem. Sci*, 8: 6988-6996.
- Zhang, S. 2017. Study of fluorine-doped tin oxide (FTO) thin films for photovoltaics applications (Doctoral dissertation, Université Grenoble Alpes (ComUE)).
- Zhou, K., Guo, Z., Liu, S. and Lee, J. H. 2015. Current approach in surface plasmons for thin film and wire array solar cell applications. *Materials*, 8(7): 4565-4581.

## **CURRICULUM VITAE**

### **Personal Information**

Name and Surname : Sabah Noori Abdulfattah AL-BAYATI

### **Education**

MSc Çankırı Karatekin University  
Graduate School of Natural and Applied Sciences 2020-Present  
Department of Physics

Undergraduate Al-Mustansiriya University  
Faculty of Science 1991-1995  
Department of Physics